Steel and Composite Structures, *Vol. 34, No. 2 (2020) 189-213*
DOI: https://doi.org/10.12989/scs.2020.34.2.189

Cyclic behaviour and modelling of stainless-clad bimetallic steels with various clad ratios

Xinpei Liu[1], Huiyong Ban[*2], Juncheng Zhu[3] and Brian Uy[1]

[1]School of Civil Engineering, Faculty of Engineering, The University of Sydney, NSW, 2006, Australia
[2]Key Laboratory of Civil Engineering Safety and Durability of China Education Ministry, Department of Civil Engineering, Tsinghua University, China
[3]School of Civil Engineering, Beijing Jiaotong University, Beijing, China

(*Received September 3, 2019, Revised November 15, 2019, Accepted November 18, 2019*)

Abstract. Stainless-clad (SC) bimetallic steels that are manufactured by metallurgically bonding stainless steels as cladding metal and conventional mild steels as substrate metal, are kind of advanced steel plate products. Such advanced composite steels are gaining increasingly widespread usage in a range of engineering structures and have great potential to be used extensively for large civil and building infrastructures. Unfortunately, research work on the SC bimetallic steels from material level to structural design level for the applications in structural engineering field is very limited. Therefore, the aim of this paper is to investigate the material behaviour of the SC bimetallic steels under the cyclic loading which structural steels usually could encounter in seismic scenario. A number of SC bimetallic steel coupon specimens are tested under monotonic and cyclic loadings. The experimental monotonic and cyclic stress-strain curves of the SC bimetallic steels are obtained and analysed. The effects of the clad ratio that is defined as the ratio of the thickness of cladding layer to the total thickness of SC bimetallic steel plate on the monotonic and cyclic behaviour of the SC bimetallic steels are studied. Based on the experimental observations, a cyclic constitutive model with combined hardening criterion is recommended for numerical simulation of the cyclic behaviour of the SC bimetallic steels. The parameters of the constitutive model for the SC bimetallic steels with various clad ratios are calibrated. The research outcome presented in this paper may provide essential reference for further seismic analysis of structures fabricated from the SC bimetallic steels.

Keywords: bimetallic steels; stainless-clad; monotonic; cyclic; constitutive model; clad ratio

1. Introduction

With development of metallurgical industries, a variety of high-performance (HP) structural steels, such as stainless steel (Gardner 2019, Baddoo 2008, Dai and Lam 2010, Theofanous and Gardner 2012, Yang *et al.* 2016, Yousefi *et al.* 2016, Averseng *et al.* 2017, Liao *et al.* 2017, Huang and Young 2018, Wang *et al.* 2019, He and Zhao 2019, Li *et al.* 2019, Cai and Young 2019, Han *et al.* 2019, Liu *et al.* 2019b), low-yield-point steel (Zirakian and Zhang 2015, Xu *et al.* 2016, He *et al.* 2016, Ma *et al.* 2018) and aluminium alloy (Su *et al.* 2014, Guo *et al.* 2015, Feng *et al.* 2018, Su *et al.* 2019), have been produced and applied in practical engineering. Despite their high-performance features in various aspects, the production cost of these pure HP steels is much higher than that of the conventional mild (CM) steel, which limits their practical applications to some extent. Accordingly, with the evolution of technologies, bimetallic steels with excellent performance and relative low cost have been developed (Ban and Shi 2018, Ban *et al.* 2019). The bimetallic steels are advanced composite steel plate products which consist of two different metals being bonding together commonly through hot-rolling process (Smith 2012). Normally the structural carbon steel particularly the CM steel is used for substrate metal and the HP steel or special purpose metal is adopted for cladding layer, as is shown in Fig. 1. Among different categories of the bimetallic steels, stainless-clad (SC) bimetallic steels manufactured by metallurgically bonding the stainless steel and the CM steel are one of the most commonly used types. The SC bimetallic steels could take advantages of the weldability, formability, thermal conductivity and the good mechanical properties of the CM steels and the excellent corrosion-resistance performance of the stainless steels in a symbiotic fashion. They are also competitive in economy due to the low production cost of the CM steel substrate and the low maintenance cost ensured by the stainless steel cladding layer. The SC bimetallic steels possess structural performance, environmental and economic benefits and are gaining increasingly widespread usage in a range of engineering structures. Previously, the SC bimetallic steels have been applied wisely in petrochemical industries or ship engineering and been employed for building curtain walls and bridge decking system (Ban *et al.* 2017). However, due to genuine lack of knowledge on the SC bimetallic steels from material level to structural design level in structural engineering area, the applications of the SC bimetallic steels in large civil and building infrastructures as structural

*Corresponding author, Ph.D.
E-mail: banhy@tsinghua.edu.cn

ISSN: 1229-9367 (Print), 1598-6233 (Online)

steel are still in its infancy. Thus, research work on the SC bimetallic steels for the applications in structural engineering field is much needed.

As has been known, civil and building infrastructures are subjected to cyclic loading in earthquakes. Understanding the cyclic behaviour of structural steels is very crucial for determining the performance of structural members and systems fabricated from the structural steels under seismic action. Developing an appropriate constitutive model that can describe the cyclic stress–strain relationship of the structural steels and can be suitable for incorporation into the numerical simulation, is beneficial for seismic analysis of structures in structural design. Abundant research work has been undertaken for studying the cyclic behaviour of the structural steels such as mild steel (Usami *et al.* 2000, Shi *et al.* 2011, Jia *et al.* 2013, Zhou *et al.* 2015, Hu *et al.* 2016, Hu *et al.* 2018), high strength steel (Dusicka *et al.* 2007, Shi *et al.* 2012, Wang *et al.* 2015, Javidan *et al.* 2017, Ho *et al.* 2018, Hai *et al.* 2018), stainless steel (Nip *et al.* 2010, Wang *et al.* 2014, Zhou and Li 2016), low-yield-point steel (Xu *et al.* 2016, Wang *et al.* 2017, Shi *et al.* 2018) and aluminium alloy (De Matteis *et al.* 2012, Guo *et al.* 2018). Constitutive models have been proposed for specific types of the structural steels. It has been indicated from the existing research that the cyclic behaviour of the structural steels is usually quite different from their monotonic behaviour, and different types of the structural steels exhibit different characteristics under cyclic loading. However, as a new type of advanced structural steel, few studies with respect to the SC bimetallic steels has been reported.

The purpose of this paper is to present an experimental study for investigating the cyclic behaviour of the SC bimetallic steels. A number of coupon specimens are tested under different monotonic and cyclic loading protocols. The monotonic and cyclic stress-strain curves of the SC bimetallic steels are obtained and discussed. The experimental results of two forms of the SC bimetallic steels with different clad ratios are compared and the differences in their monotonic and cyclic behaviour are identified. It is worth noting that the clad ratio is defined as the ratio of the thickness of cladding layer to the total thickness of SC bimetallic steel plate. The value of the clad ratio can be between 0 and 1. Two different clad ratios that are not greater than 0.5 and in the practical common range of clad ratio for economic considerations are selected for comparison in the experimental study. Based on the experimental observations, a cyclic constitutive model with combined hardening criterion is recommended for numerical simulation of cyclic behaviour of the SC bimetallic steels. The parameters of the constitutive model for the SC bimetallic steels with various clad ratios are calibrated based on the cyclic loading test results obtained by using an experimentally validated two-layer finite element model. The accuracy of the recommended constitutive model with the calibrated parameters are verified by comparing the results of its simulation with the numerical results obtained from the two-layer finite element model for a wide range of loading protocols.

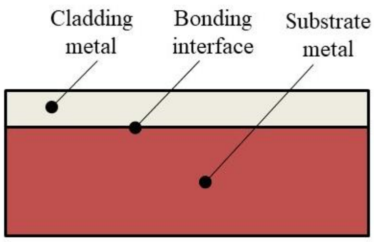

Fig. 1 Illustration of bimetallic steel

2. Experimental study

2.1 Description of experiment

To study the cyclic stress-strain behaviour of the stainless-clad (SC) bimetallic steels, a series of experimental cyclic loading tests on cyclic coupons were undertaken, with a variety of loading protocols being incorporated. Design of test specimens took the clad ratio β into account. Two main groups of specimens with different clad ratios β = 0.375 and 0.5 (or saying 3/8 and 3/6) were tested. The experimental results of the cyclic loading tests for the SC bimetallic steel with β = 0.375 can be found in the literature (Zhu *et al.* 2018) reported by the authors. In this paper, the experimental programme, experimental observations and test results for the SC bimetallic steel with β = 0.5 are presented in detail, and the experimental results of the monotonic and cyclic loading tests for the SC bimetallic steels with different clad ratios are compared and discussed.

The SC bimetallic steel plates discussed in this paper were all fabricated through hot-rolling process (GB/T 8165 2008) by using 316L austenitic stainless steel (CECS 410 2015) as the cladding layer and Q235B steel (GB/T 700 2006) as the substrate metal. The nominal thickness of both the cladding and substrate layers of the tested SC bimetallic steel plate with β = 0.5 were chosen to be 3 mm. The chemical compositions of two components forming the SC bimetallic steel plates are presented in Table 1. The cyclic coupons with reduced section were cut from the SC bimetallic steel plates for testing. The cutting direction was perpendicular to the rolling direction for steel plates, since such coupon usually can provide more conservative experimental results. The geometric dimensions of the cyclic coupons are shown in Fig. 2, which were designed to fit in the testing machine and instrumentation with reference to the British standard BS7270 (2016). In order to avoid or postpone buckling of the coupon in compression, the effective length and width of the reduced section part of test specimens were designed to be 13 and 18 mm, respectively, resulting in the relatively small length-to-width ratio being 0.72. The reduced section parts and transition zones of the test specimens were machined using numerically controlled equipment for preventing undercutting. All the testings on the coupon specimens were conducted by using a universal fatigue testing machine Instron 8801, as shown in Fig. 3. Hydraulic grips were used to mount the specimen such that both tension and compression loadings could be applied. An extensometer with a gauge length of 12.5 mm was utilised

Table 1 Chemical compositions of 316L authentic stainless steel and Q235B mild steel

Materials	Elements (%)							
	C	Mn	Si	P	S	Als	Ni	Cr
316L austenitic stainless steel	0.057	1.20	0.45	0.015	0.005	0.038	10.5	16.91
Q235B mild steel	0.15	1.10	0.25	0.010	0.004	0.037	-	-

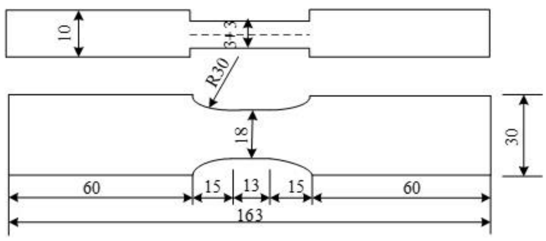

Fig. 2 Geometric dimensions of bimetallic steel coupons (Unit: mm)

Fig. 3 Photo of testing machine

for measuring the longitudinal displacements within the effective length of the coupons so that the engineering strain values could be obtained from the measured displacements divided by 12.5 mm. The maximum strain measurement range for the extensometer is ±40%. Uniaxial force was applied on the coupon specimens by using strain-controlled method achieved through the measured data from the extensometer in order to eliminate the effect of possible grip slippage or deformation outside the effective length. Loads, strains, and displacements were all recorded using the data acquisition systems.

A variety of loading protocols were adopted in the testings. The selection of loading protocols referred to the previous similar cyclic loading tests (Shi *et al.* 2012, Wang *et al.* 2017, Shi *et al.* 2018) and the selected loading protocols represented the typical simplified scenarios that the structural steels may encounter in earthquake actions. A total of 17 various loading protocols were adopted for 23 specimens. The 17 loading protocols included monotonic tensile and compressive loadings as well as 15 different triangular waveform cyclic loadings with stepwise, constant, multi-steps and random strain amplitudes. The spectrums of the load protocols LP1-17 are illustrated in Fig. 4 and described in Table 2. For the monotonic loading protocols LP1 and LP2, three coupon specimens were prepared and tested subjected to tensile force, and three were subjected to compressive force. For the cyclic loading protocols LP3 to LP17, one coupon specimen was prepared and tested under each cyclic loading protocol expect for the loading protocols LP3 and LP4 under each of which two coupon specimens were prepared and the same tests were undertaken repeatedly. Therefore, in this paper, the nomenclature of the test specimens was not only based on the nominal thickness of the substrate metal and cladding layer of the specimens, but also considered the adopted loading protocols. For instance, Specimen S3-C3-LP3 (1) indicated a SC bimetallic steel coupon with a 3 mm-thick Q235 steel substrate (S) metal and a 3 mm-thick 316L stainless steel cladding (C) layer, which were tested subjected to the loading protocol LP3. The last number inside the bracket in the designation of Specimen S3-C3-LP3 (1) denoted that this was the first specimen in a group of specimens with identical geometric dimensions and subjected to same loading protocol. To minimise the influence of temperature increase caused by the rapid working of material through inelastic strains, the strain rate for the monotonic loading tests was set to be 0.025%/s in accordance with the Chinese standards GB/T228.1 (2010) while the strain rate for the cyclic loading protocol LP3-16 was set to be 0.1%/s (Zhou *et al.* 2015). The applied strain rates for the random cyclic loading protocol LP17 were determined based on the calculated strain history at the bottom flange of a steel beam in a steel frame subjected to an irregular seismic loading (Hu 2016).

Table 2 Descriptions of loading protocols

Protocols	Descriptions
LP1	Monotonic tensile loading
LP2	Monotonic compressive loading
LP3	Specimen is loaded with symmetrically and gradually increasing strain amplitudes; amplitude of each increment is 0.2%; loading cycles 1 time at each increment level; tensile loading is applied prior to compressive loading at each cycle.
LP4	Specimen is loaded with symmetrically and gradually increasing strain amplitudes; amplitude of each increment is 0.2%; loading cycles 1 time at each increment level; compressive loading is applied prior to tensile loading at each cycle.
LP5	Specimen is loaded with symmetrically and gradually increasing strain amplitudes; amplitude of each increment is 0.2%; loading cycles 2 times at each increment level; tensile loading is applied prior to compressive loading at each cycle.
LP6	Specimen is loaded with symmetrically and gradually increasing strain amplitude; amplitude of each increment is 0.2%; loading cycles 2 times at each increment level; compressive loading is applied prior to tensile loading at each cycle.
LP7	Specimen is loaded with gradually increasing strain amplitudes in tensile direction and fixed strain amplitude in compressive direction; amplitude of each increment in tensile direction is 0.5%; amplitude in compressive direction is fixed at 0.0%; tensile loading is applied prior to compressive loading at each cycle.
LP8	Specimen is loaded with gradually increasing strain amplitudes in tensile direction and fixed strain amplitude in compressive direction; amplitude of each increment in tensile direction is 0.5%; amplitude in compressive direction is fixed at -1.0%; tensile loading is applied prior to compressive loading at each cycle.
LP9	Specimen is loaded with gradually increasing strain amplitudes in compressive direction and fixed strain amplitude in tensile direction; amplitude of each increment in compressive direction is 0.2%; amplitude in tensile direction is fixed at 4.0%; tensile loading is applied prior to compressive loading at each cycle.
LP10	Specimen is stretched to 0.5% tensile strain in advance and then is loaded with 0.5% tensile strain axis-symmetrically and gradually increasing strain amplitudes; amplitude of each increment is 0.5%; tensile loading is applied prior to compressive loading at each cycle.
LP11	Specimen is stretched to 3.5% tensile strain in advance and then is loaded with 3.5% tensile strain axis-symmetrically and gradually increasing strain amplitudes; amplitude of each increment is 0.5%; tensile loading is applied prior to compressive loading at each cycle.
LP12	Specimen is loaded with symmetrically and constant strain amplitudes of 2%; loading cycles 10 times; tensile loading is applied prior to compressive loading at each cycle.
LP13	Specimen is loaded with symmetrically and constant strain amplitudes of 2%; loading cycles 20 times; tensile loading is applied prior to compressive loading at each cycle.
LP14	Specimen is loaded with symmetrically and constant strain amplitudes of 2% for 20 cycles followed by being loaded with strain amplitudes of 3% for one more cycle; tensile loading is applied prior to compressive loading at each cycle.
LP15	Specimen is loaded with symmetrically and gradually decreasing strain amplitudes; initial strain amplitude is 3.0%, amplitude of each decrease is 0.5%; tensile loading is applied prior to compressive loading at each cycle.
LP16	Specimen is loaded under triangular waveform cyclic loading with fixed absolute value of cyclic strain range of 4.0%; initial tensile strain amplitude is 2.0%, tensile strain amplitude increases gradually; amplitude of each increment is 0.5%; tensile loading is applied prior to compressive loading at each cycle.
LP17	Random cyclic loading

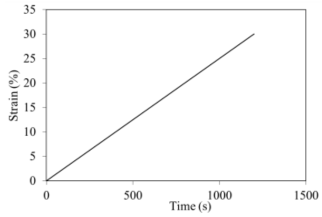

(a) LP1

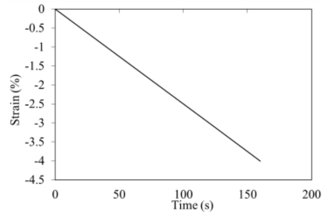

(b) LP2

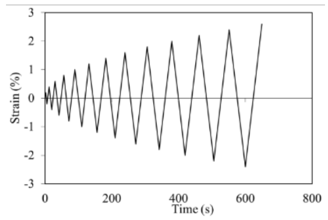

(c) LP3

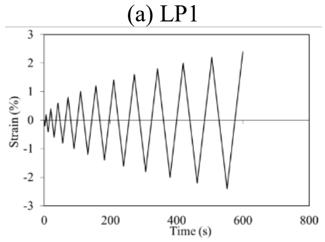

(d) LP4

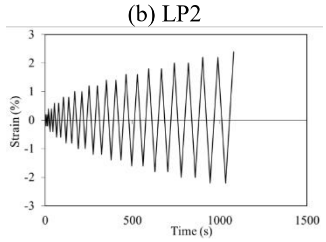

(e) LP5

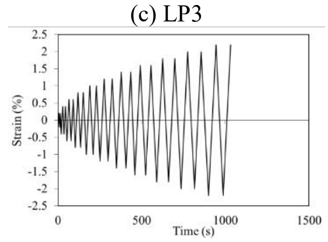

(f) LP6

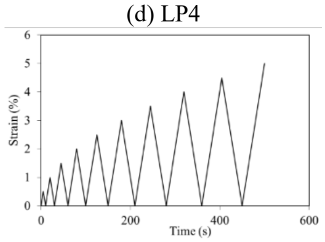

(g) LP7

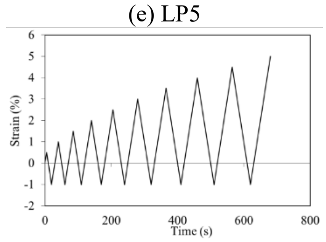

(h) LP8

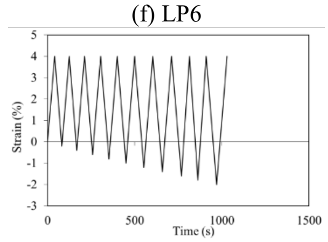

(i) LP9

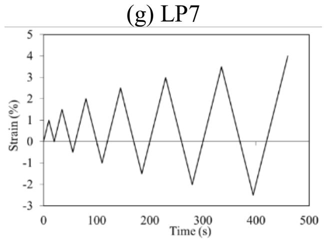

(j) LP10

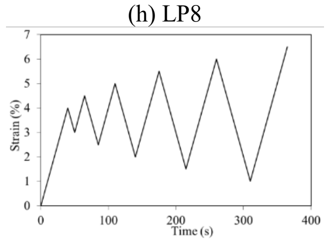

(k) LP11

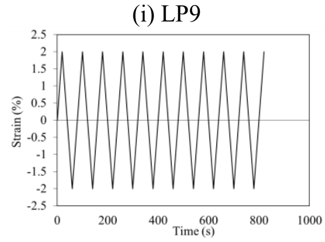

(l) LP12

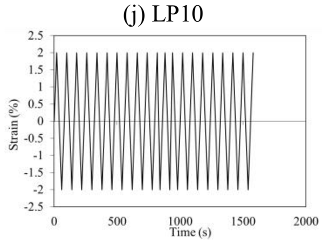

(m) LP13

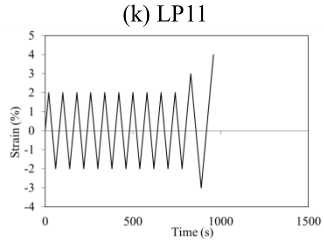

(n) LP14

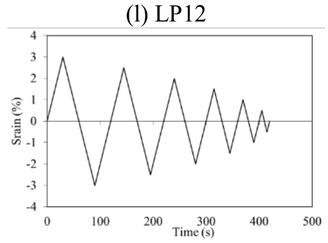

(o) LP15

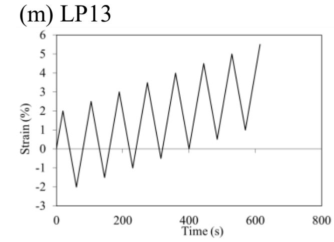

(p) LP16

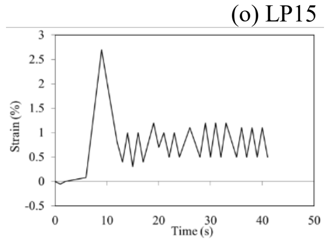

(q) LP17

Fig. 4 Spectrums of loading protocols

2.2 Monotonic behaviour

Two typical failure modes viz. fracture in tension and buckling in compression, were identified on the coupon specimens under monotonic loading. When the specimen was tested under monotonic tensile force, significant necking phenomenon at the reduced section part could be observed, after the maximum tensile stress on the specimen was attained. No separation between the cladding layer and substrate metal was recognised, which illustrated the collaborative performance of two component layers of the SC bimetallic steel plate under sustained tensile force. At the end of monotonic tensile loading test, the fracture of specimen took place immediately after the two component layers of the SC bimetallic steel plate separated from each other as shown in Fig. 5(a). Fractured surfaces of the coupon specimens after the monotonic tensile loading tests were examined by scanning electron microscopy (SEM).

(a) Delamination before fracture (b) Local buckling (after unloading)

Fig. 5 Failure modes of coupon specimens

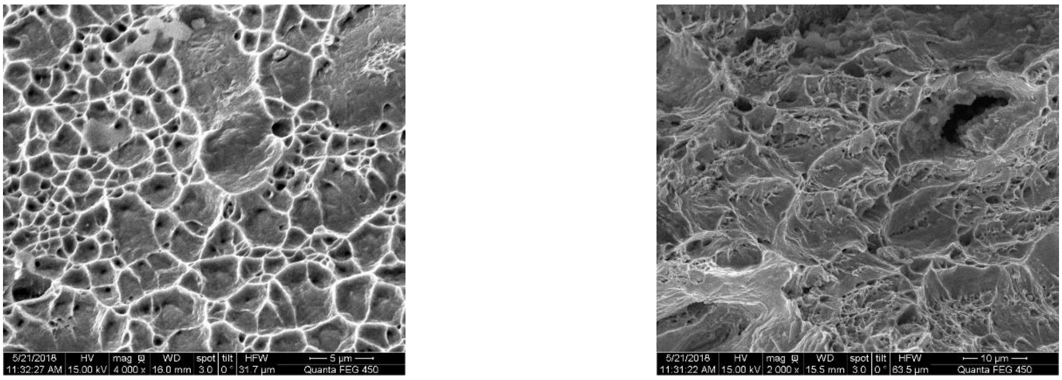

(a) 316L austenitic stainless steel layer (b) Q235B mild steel layer

Fig. 6 SEM images of interfacial fractography

The typical SEM images of interfacial fractography of the two component layers are shown in Fig. 6. Many round and ellipse dimples observed on the fractured surfaces suggested a ductile fracture failure of the SC bimetallic steel specimens under monotonic tensile loading. When the specimens were tested under monotonic compressive force, buckling failure as shown in Fig. 5(b) was recognised. The monotonic compressive loading tests were stopped prematurely when the buckling occurred. Consequently, the ductility of steel in compression was compromised by the buckling behaviour, but this behaviour corresponded to the response in structural level rather than that in material level.

Fig. 7 shows the measured monotonic stress-strain curves of the SC bimetallic steels with β = 0.5. The values of key parameters obtained from the monotonic stress-strain curves are listed in Table 3, which provides the values of the elastic modulus E, 0.2% proof stress $\sigma_{0.2}$, strain corresponding to 0.2% proof stress $\varepsilon_{0.2}$ and the ultimate strength f_u. It should be noted that during the monotonic tensile loading tests, the extensometer was removed from the specimens when the measured strain reached 30% due to the limitation of the equipment, so the fracture stress and strain values for each specimen were unable to be recorded. During the monotonic compressive loading tests, the extensometer was removed at a compressive strain of around 3% when obvious buckling deformations were recognised on the test specimens, so the compressive stress-strain curves beyond the strain of 3% particularly the ultimate compressive strength values were missed. It can be seen from Fig. 7 that the monotonic stress-strain curves of the SC bimetallic steels displayed the characteristics of the typical nonlinear stress-strain curve which is lack of a noticeable yield plateau. The 0.2% proof stress $\varepsilon_{0.2}$ that corresponds to a plastic strain of 0.2% (Ramberg and Osgood 1943) was used to define the yield strength f_y for the SC bimetallic steels. The SC bimetallic steels showed good ductility under monotonic tensile loading, as the measured strains corresponding to the ultimate strength were located in the range between 20% and 25%. Compared with the tensile stress-strain curves, the compressive stress-strain curves exhibited higher stress values at strain hardening stage of the stress-strain curve beyond the yield strength points, although both monotonic stress-strain curves almost overlapped at the elastic stage. This might be because the cross-section area of the specimen was enlarged significantly at the hardening stage when the specimen was subjected to uniaxial compressive loading, but the obtained engineering stress value was calculated from the compressive force divided by the original cross-section area of the specimen. This resulted in a larger calculated

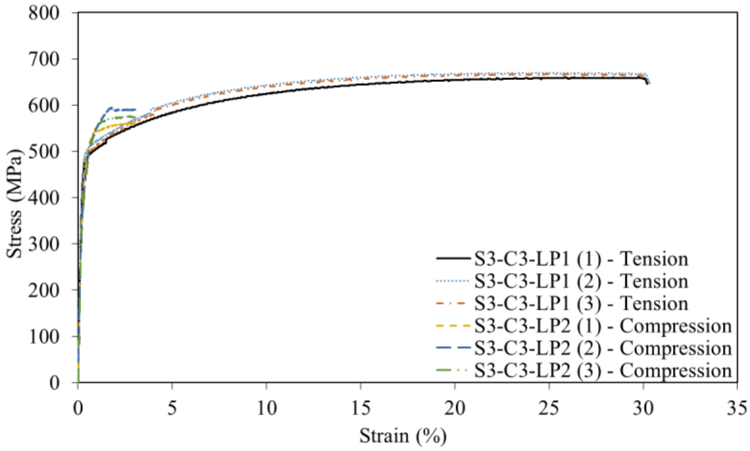

Fig. 7 Monotonic stress-strain curves

Table 3 Key parameters values from measured monotonic stress-strain curves

Specimens	E (GPa)	$\sigma_{0.2}$ or f_y (MPa)	$\varepsilon_{0.2}$ (%)	f_u (MPa)
S3-C3-LP1 (1)	221.4	481.9	0.418	659.7
S3-C3-LP1 (2)	254.7	494.9	0.395	669.8
S3-C3-LP1 (3)	212.5	484.7	0.426	667.1
Average*	217.0	483.3	0.422	663.4
S3-C3-LP2 (1)	206.1	476.7	0.431	-
S3-C3-LP2 (2)	221.2	448.1	0.405	-
S3-C3-LP2 (3)	200.5	446.2	0.422	-
Average	209.3	457.0	0.419	-

*Note: The measured elastic modulus E of Specimen S3-C3-LP1 (2) is overlarge which could be due to slight slippage o f extensometer in the experiment, so this data wasn't used for calculating the averaged value

compressive stress value compared with the tensile stress one. It is summarised from Table 3 that the average measured values of E, f_y and f_u for the SC bimetallic steels with β = 0.5 are 213GPa, 468MPa and 663MPa, respectively. With respect to detailed material properties of the component stainless steel and carbon steel for the SC bimetallic steels herein, the authors have carried out separate tensile coupon tests (Ban *et al*. 2019) with specific data being given.

2.3 Cyclic behaviour

Fig. 8 depicts the measured cyclic stress-strain curves of the SC bimetallic steels with β = 0.5 for most of the loading protocols shown in Fig. 4 and described in Table 2. The cyclic stress-strain curve for the loading protocol LP5 is not provided because of the test data error caused by the unexpected slippage of extensometer during the testing. As is shown in Fig. 8, all specimens achieved quite plumb and stable cyclic loops, indicating their good seismic performance and energy dissipation capacities. It was observed during the experimental testings that two component layers of the SC bimetallic steels behaved collaboratively as a whole plate under the cyclic loading, and none of the separation between two component layers or the fracture of specimen occurred for every cyclic loading protocol case. The well-known Bauschinger effect can also be noticed in the measured cyclic stress-strain curves, as the increase in the maximum stress of the prior tension or compression loading cause an expense of the yield strength of the subsequent reverse loading.

Among all loading protocols, the loading protocols LP3 and LP4 as shown in Figs. 4(c) and 4(d) which consisted of symmetrically and monotonically increasing strain amplitudes with one cycle at each level, were regarded as the most classic and mainly used cyclic loading protocols. It can be seen from the cyclic curves (Figs. 8(a)-8(d)) for the specimens tested under these protocols that the maximum stresses of both tension and compression loading increased with the increase in cyclic strain amplitude, which is identified as strain hardening. The strain hardening of a material under cyclic loading can be associated with an isotropic hardening, a kinematic hardening or both (Silvestre *et al.* 2015, Sim and Hughes 1998). It can be seen that the hardening behaviour of the SC bimetallic steels exhibited combined isotropic and kinematics hardening characteristics. In first few cycles with small strain amplitudes, obvious isotropic hardening behaviour was observed in the cyclic stress-strain curves. However, in the following cycles with moderate and large strain amplitudes,

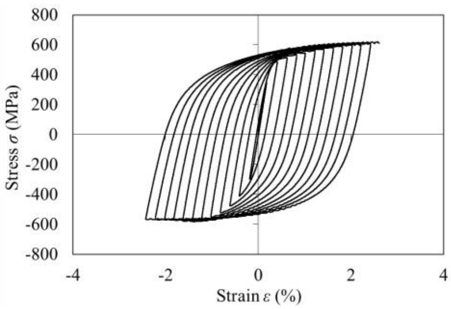

(a) S3-C3-LP3 (1)

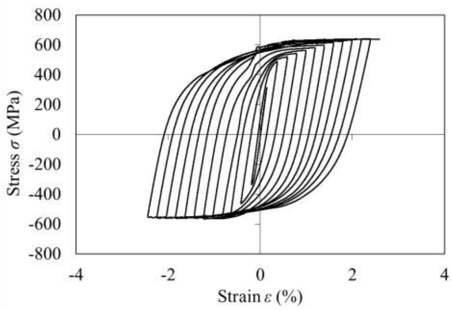

(b) S3-C3-LP3 (2)

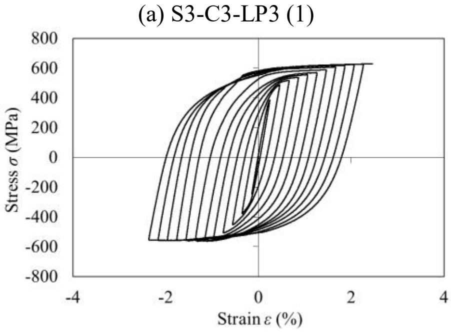

(c) S3-C3-LP4 (1)

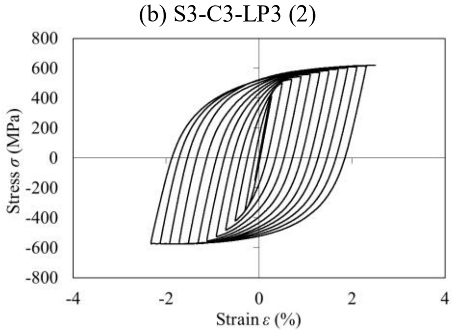

(d) S3-C3-LP4 (2)

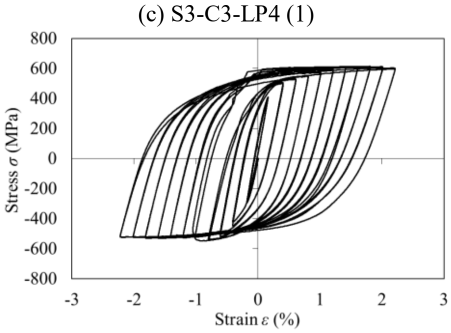

(e) S3-C3-LP6

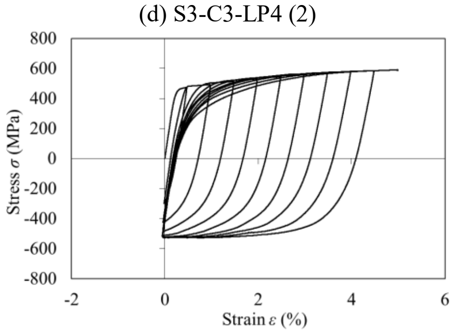

(f) S3-C3-LP7

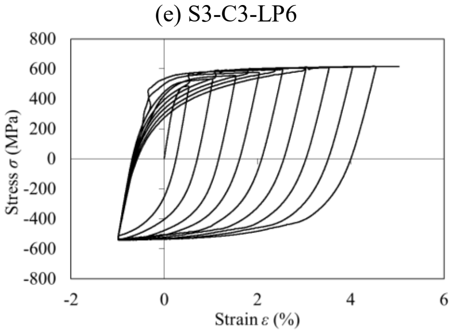

(g) S3-C3-LP8

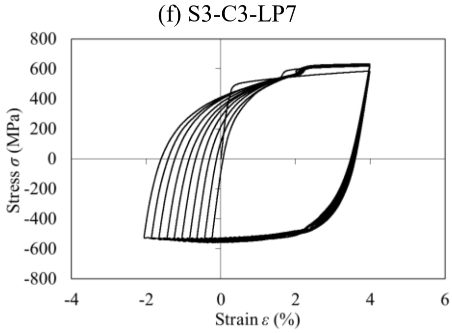

(h) S3-C3-LP9

Continued-

the isotopic hardening developed gently and then shortly tended to be steady when the kinematic hardening became the dominating hardening behaviour. The isotropic and kinematic hardening behaviour of the SC bimetallic steels can be further illustrated in Figs. 8(k) and 8(l), in which the cyclic loading protocols LP12 and LP13 (Figs. 4(l) and 4(m)) with constant and relatively large strain amplitudes were considered. Similar as the observations from Figs. 8(a)-(d), the cyclic curves in Figs. 8(k) and 8(l) displayed obvious isotropic hardening behaviour at initial but arrived at full saturation rapidly in just a few complete cycles. This trend is demonstrated quantitively in Fig. 9 which depicts the changes in the maximum tensile stress of each cycle through cyclic loading life. The fully saturated stress-strain curves showed in Figs. 8(k) and 8(l) also clearly indicated the nonlinear kinematic hardening behaviour of the SC bimetallic steels under cyclic loading. The combined isotropic and kinematics hardening characteristics of the SC bimetallic steels under cyclic loading can also be recognised on the other cyclic stress-strain curves in Fig. 8 even though the strain amplitudes might not be applied symmetrically in these cases.

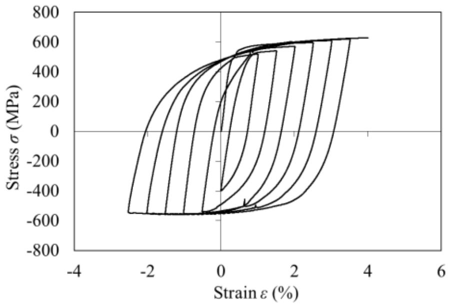

(i) S3-C3-LP10

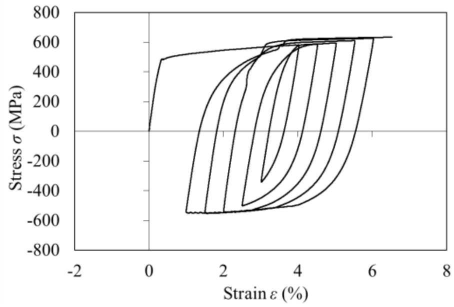

(j) S3-C3-LP11

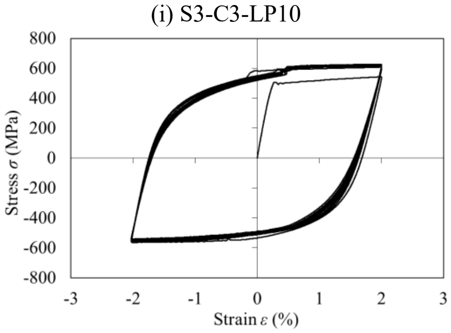

(k) S3-C3-LP12

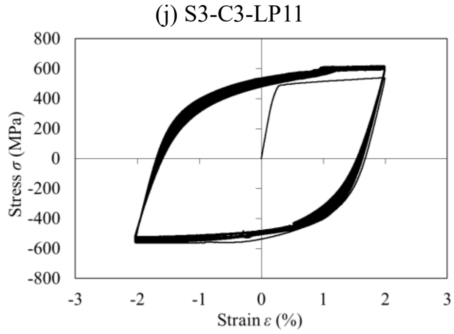

(l) S3-C3-LP13

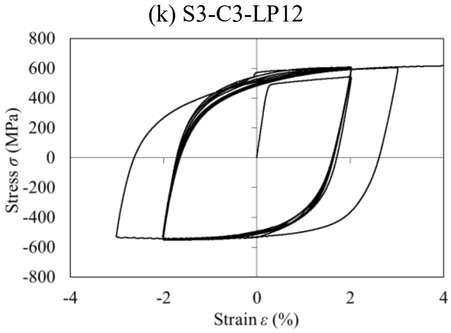

(m) S3-C3-LP14

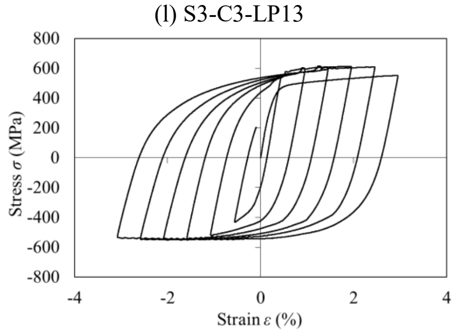

(n) S3-C3-LP15

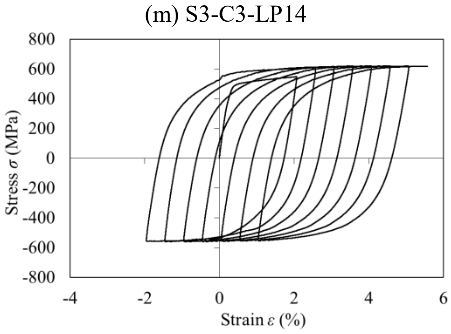

(o) S3-C3-LP16

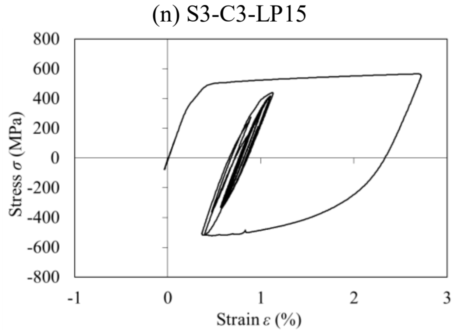

(p) S3-C3-LP17

Fig. 8 Cyclic stress-strain curves

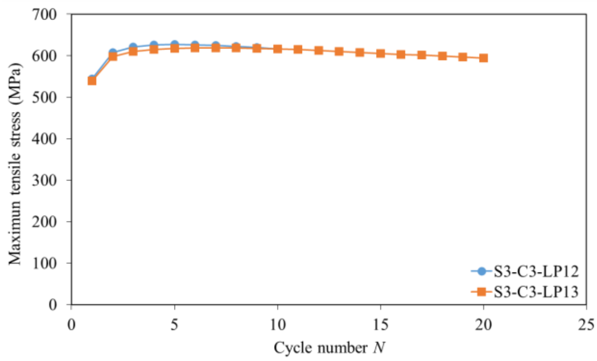

Fig. 9 Relationship of maximum cyclic tensile stress and cycle number

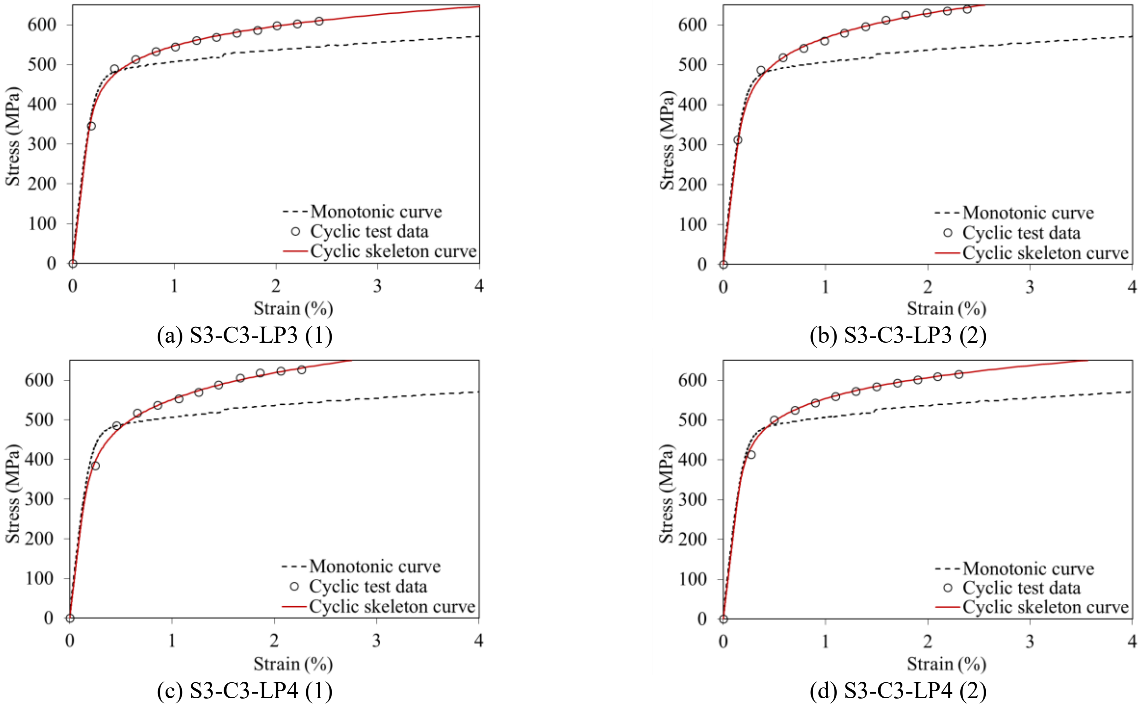

Fig. 10 Cyclic skeleton curves

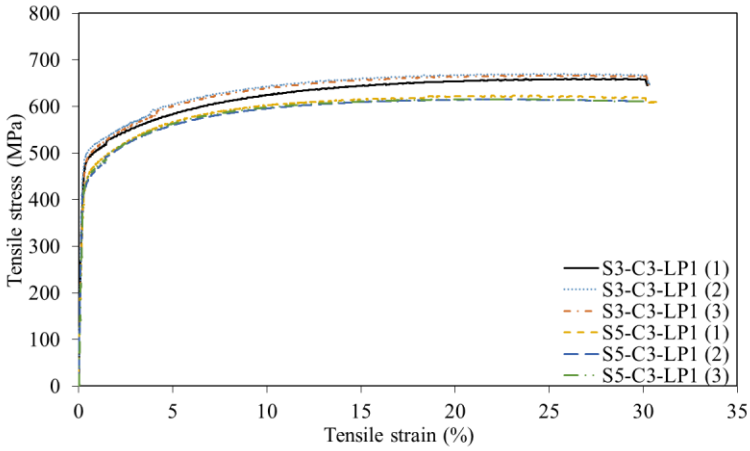

Fig. 11 Comparisons of monotonic curves for SC bimetallic steels with different clad ratios

2.4 Cyclic skeleton curve

To investigate and quantify the difference in material response under monotonic and cyclic loadings, the cyclic skeleton curves of the SC bimetallic steels with β = 0.5 were obtained and compared with the corresponding monotonic stress-strain curves. The cyclic skeleton curves were generated by tracing the maximum cyclic stress point at each applied strain amplitude. The cyclic skeleton curves without a distinct yield point usually can be simulated by using the Ramberg-Osgood model (1943). This model contains an exponential-form function with three material-dependent parameters, which is given by

$$\varepsilon = \frac{\sigma}{E} + \left(\frac{\sigma}{K'}\right)^{\frac{1}{n'}} \tag{1}$$

where σ and ε are the stress and strain in the cyclic skeleton curves, respectively. Three material-dependent parameters are the elastic modulus E, hardening coefficient K' and the hardening exponent n'. While the elastic modules E was determined by using the measured average elastic modulus from the monotonic loading tests, the parameters K' and n' of the Ramberg-Osgood model were calibrated through fitting the experimental cyclic skeleton curves of the specimens tested under the load protocols LP3 and LP4. Fig. 10 shows the comparisons of the cyclic skeleton curves developed using the calibrated Ramberg-Osgood model

Table 4 Calibrations of Ramberg-Osgood model parameters

Specimens	hardening coefficient K'	hardening exponent n'
S3-C3-LP3 (1)	909.9	0.104
S3-C3-LP3 (2)	1028.3	0.121
S3-C3-LP4 (1)	1084.2	0.138
S3-C3-LP4 (2)	940.7	0.108
Average	990.8	0.118

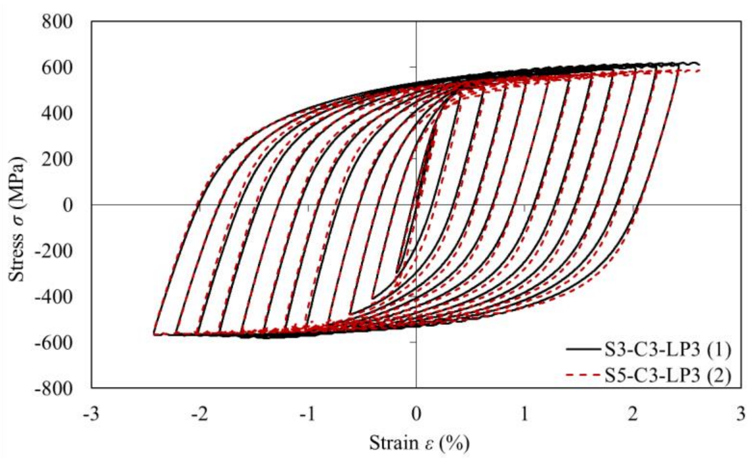

Fig. 12 Comparison of cyclic curves for SC bimetallic steels with different clad ratios

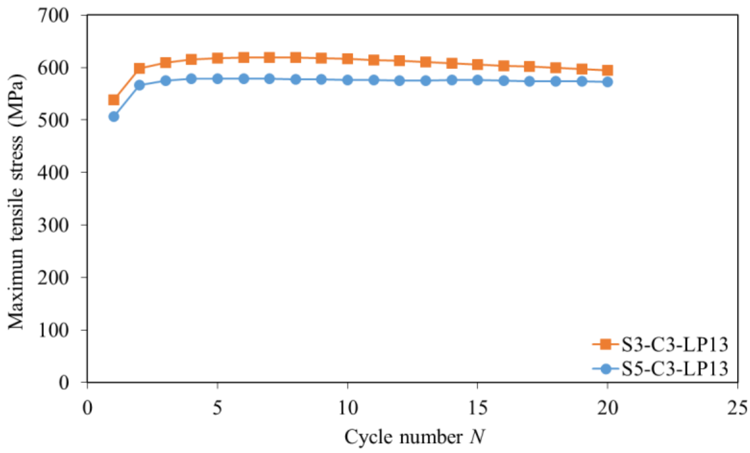

Fig. 13 Comparison of isotropic hardening trend for SC bimetallic steels with different clad ratios

with the monotonic and cyclic test results. It can be seen that the simulated cyclic skeleton curves based on the Ramberg-Osgood model had good agreement with the cyclic test results. Large differences between the cyclic skeleton curves and the monotonic stress-strain curves particularly in the plastic strain range were observed. The stresses in the cyclic skeleton curves were improved by up to 18% compared with the monotonic stress within the strain amplitudes of 2.5%.

2.4 Comparisons of SC bimetallic steels with different clad ratios

In this section, the experimental results of the monotonic and cyclic loading tests for the SC bimetallic steels with β = 0.5 are compared with those for the SC bimetallic steels with β = 0.375. The SC bimetallic steel plates with β = 0.375 were formed by using 3 mm thick 316L austenitic stainless steel plate as the cladding layer and 5 mm thick Q235B steel plate as the substrate metal. 23 coupon

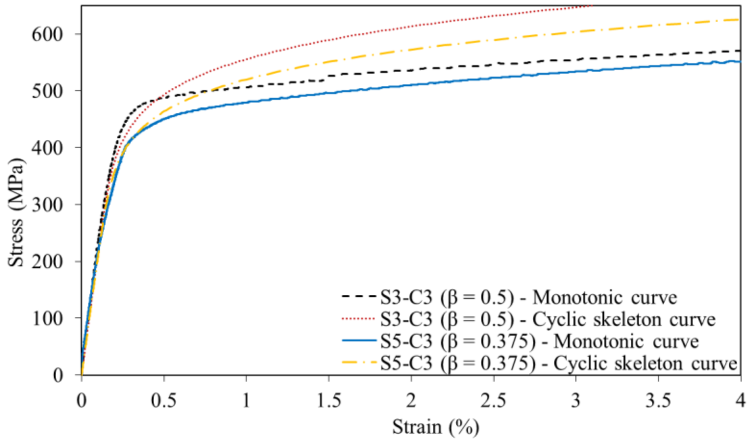

Fig. 14 Comparison of cyclic skeleton curves for SC bimetallic steels with different clad ratios

specimens were fabricated and tested under the 17 loading protocols shown in Fig. 4 and described in Table 2. The details of the experiment on the SC bimetallic steels with β = 0.375 were given in the literature (Zhu *et al.* 2018) presented by the authors. Fig. 11 shows the comparisons of the measured monotonic tensile stress-strain curves for the SC bimetallic steels with β = 0.5 and 0.375. It can be seen that Specimens S3-C3-LP1 (1)-(3) with β = 0.5 had higher yield strength and ultimate strength than Specimens S5-C3-LP1 (1)-(3) with β = 0.375. This could be attributed to the reason that the yield strength and ultimate strength of the cladding layer material 316L austenitic stainless steel were higher than those of the substrate metal material Q235B steel. This observation was consistent with the findings reported in the reference (Liu *et al.* 2019a) on the titanium-clad bimetallic steels.

The comparisons of the measured cyclic stress-strain curves for the SC bimetallic steels with β = 0.5 and 0.375 under the same loading protocol LP3 are shown in Fig. 12. Apparently, the cyclic stress-strain curve of Specimen S3-C3-LP3 (1) with β = 0.5 was much wider than that of Specimen S5-C3-LP3 (2) with β = 0.375. The difference was very noticeable in the first few cycles of the stress-strain curves. At the last cycle with strain amplitude of 2.5%, the maximum tensile stress of Specimen S3-C3-LP3 (1) is 45 MPa higher than that of Specimen S5-C3-LP3 (2). The combined isotropic and kinematic hardening behaviour can be observed on both the cyclic stress-strain curves of the SC bimetallic steels with different clad ratios. Fig. 13 compares the relationship of the maximum tensile stress of each cycle and the cycle number extracted from the cyclic stress-strain curves of Specimens S3-C3-LP13 and S5-C3-LP13 under the same constant strain amplitude loading protocol. It is shown that the trend of the isotropic hardening for these two SC bimetallic steels were quite similar as the maximum cyclic stress amplitudes got to a stable state rapidly in just a few complete cycles. The comparisons of the cyclic skeleton curves with the monotonic stress-strain curves for the SC bimetallic steels with β = 0.5 and 0.375 are depicted in Fig. 14. The cyclic skeleton curves were obtained by using Eq. (1), in which the values of three model parameters E, K' and n' were determined by using the average values of the measured or calibrated data from the corresponding experimental tests. It is observed that the improvement of the stress in the cyclic skeleton curves compared with the monotonic stress for the SC bimetallic steels with β = 0.5 could be more significant than that for the SC bimetallic steels with β = 0.375. For example, at strain amplitude of 2%, the stress in the cyclic skeleton curves increased by 14% compared with the monotonic stress for the SC bimetallic steels with β = 0.5, but the increase ratio was only 12% for the SC bimetallic steels with β = 0.375. The differences in the cyclic responses of the SC bimetallic steels with different clad ratios could be caused by the distinctive cyclic characterises of the cladding layer material 316L austenitic stainless steel and substrate material Q235B steel due to their different crystallographic structures and alloy contents (Nip *et al.* 2010).

3. Cyclic constitutive model for SC bimetallic steels with various clad ratios

3.1 Constitutive model with combined hardening criterion

To numerically simulate the cyclic behaviour of the SC bimetallic steels, a constitutive model for cyclic plasticity of the SC bimetallic steels is needed. As was observed from the experimental results, the SC bimetallic steels under cyclic loading showed the combined nonlinear isotropic and kinematic hardening behaviour and the isotropic hardening tended to gradually reach a saturation state with an increase of cumulative plastic strain. Therefore, a constitutive model for cyclic plasticity of metals considering the combined isotropic and kinematic hardening behaviour, which was proposed by Chaboche (1986, 1989) and has been implemented in the commercial finite element software ABAQUS (Hibbit *et al.* 2016), are recommended for the SC bimetallic steels. It should be noted that the recommended constitutive model for the SC bimetallic steels would only

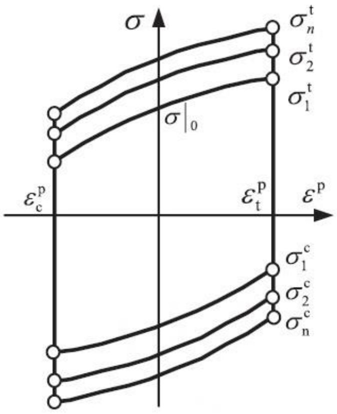

(a) Isotropic hardening component

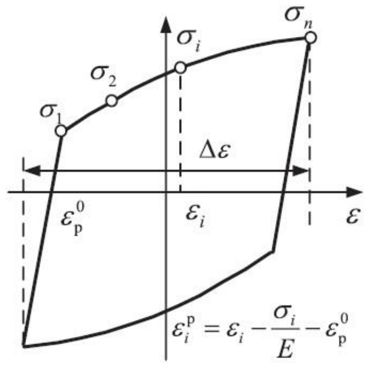

(b) Kinematic hardening component

Fig. 15 Calibrations of constitutive model parameters (Hibbit *et al.* 2016)

be applied for the most common cases in their applications that the SC bimetallic steel plate members (the thickness of the plates are significantly smaller than their other dimensions) are under the plane strains parallel to the surfaces of plates while the distributions of the plane strains throughout the plate thickness could be assumed to be uniform. In this cyclic constitutive model, the von Mises yield criterion and an associative flow rule are assumed. The combined nonlinear hardening model consists of an isotropic hardening and a kinematic hardening component. The material parameters with respect to these two hardening components can be calibrated independently according to the test data.

The isotropic hardening component gives the evolution of the yield surface size σ^0, as a function of the equivalent plastic strain $\bar{\varepsilon}^{\rm pl}$. The function is given by

$$\sigma^0 = \sigma\big|_0 + Q_\infty\left(1-e^{-b\bar{\varepsilon}^{\rm pl}}\right) \tag{2}$$

where $\sigma|_0$ is the yield stress at zero equivalent plastic strain, Q_∞ is the maximum change of the size of yield surface, and b defines the rate at which the size of the yield surface changes as the equivalent plastic strain increases. Q_∞ and b are two material parameters of the isotropic hardening component that need to be calibrated. As is indicated in Fig. 15(a), the size of the yield surface of the ith cycle can be obtained by

$$\sigma_i^0 = \left(\sigma_i^{\rm t} - \sigma_i^{\rm c}\right)\Big/2 \tag{3}$$

where $\sigma_i^{\rm t}$ and $\sigma_i^{\rm c}$ are the maximum stress in tension and compression at the ith cycle, respectively. The equivalent plastic strain $\bar{\varepsilon}_i^{\rm pl}$ corresponding to σ_i^0 can be calculated through the accumulation of the plastic strain $\varepsilon^{\rm p}$. Hence, the two material parameters Q_∞ and b of the isotropic hardening can be determined by fitting Eq. (2) to the several data pairs of (σ_i^0, $\bar{\varepsilon}_i^{\rm pl}$) including the point ($\sigma|_0$, 0) which are obtained from the test results.

The kinematic hardening component of the model defines the change of overall backstress α, which can be expressed as a function of the plastic strain $\varepsilon^{\rm p}$ that is written as

$$\alpha = \sum_{k=1}^{N} \frac{C_k}{\gamma_k}\left(1-e^{-\gamma_k\varepsilon^{\rm p}}\right) + \alpha_{k,1}e^{-\gamma_k\varepsilon^{\rm p}} \tag{4}$$

where C_k and γ_k are two material parameters of kinematic hardening component that need to be calibrated, $\alpha_{k,1}$ is the kth backstress component at the first data point and N is the number of backstress components. The parameter C_k represents the initial kinematic hardening modulus and γ_k specifies the rate at which the kinematic hardening modulus varies as the plastic strain increases. The number of backstress N is taken as an appropriate value of 2 in this paper. As is shown in Fig. 15(b), the stress and strain data (σ_i, ε_i) can be obtained from the stabilised cycle of a specimen subjected to symmetric strain cycles. Each data pair of (α_i, $\varepsilon_i^{\rm p}$) can be specified with the shift of strain axis as

$$\alpha_i = \sigma_i - \left(\frac{\sigma_1 + \sigma_n}{2}\right) \tag{5}$$

$$\varepsilon_i^{\rm p} = \varepsilon_i - \frac{\sigma_i}{E} - \varepsilon_{\rm p}^0 \tag{6}$$

where $\varepsilon_{\rm p}^0$ is the strain corresponding to the zero stress in the cycle. The calibration of the two material parameters C_k and γ_k of kinematic hardening can be realised through fitting Eq. (4) to the data pairs (α_i, $\varepsilon_i^{\rm p}$) which are obtained based on the test results.

3.2 Two-layer finite element (FE) model

Due to the fact that only two forms of the SC bimetallic steels with two different clad ratios were examined in the experimental study, a two-layer finite element (FE) model of the SC bimetallic steel coupons subjected to cyclic loading was established by using FE software ABAQUS (Hibbit *et al.* 2016), in order to extend the database on the cyclic stress-strain curves of the SC bimetallic steels

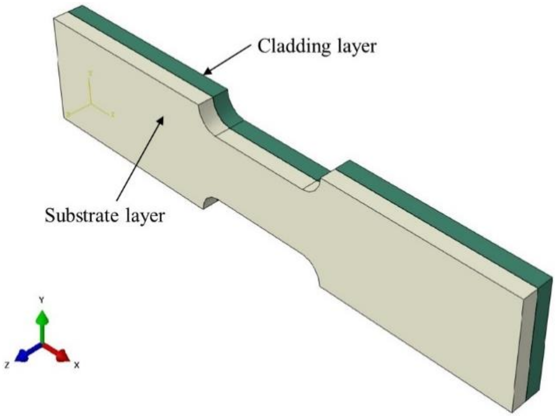

Fig. 16 Two-layer FE model

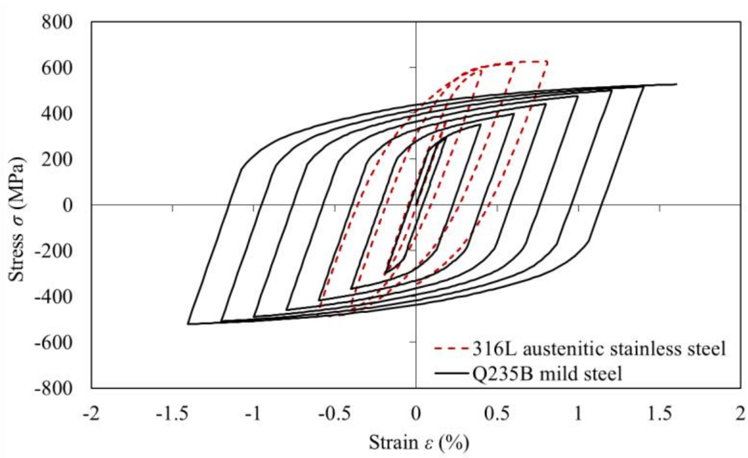

Fig. 17 Cyclic stress-strain curves of pure 316L austenitic stainless steel and Q235B mild steel

Table 5 Calibrations of constitutive model parameters for pure 316L austenitic stainless steel and Q235B mild steel

Materials	$\sigma\|_0$ (MPa)	Q_∞ (MPa)	b	C_1 (MPa)	γ_1	C_2 (MPa)	γ_2
Q235B	264	74	34	17841	109	63794	1436
316L	270	118	2800	74454	662	74454	662

considering a wide range of clad ratios. In the FE model, the coupon specimens were developed by assembling two component layers including the 316L austenitic stainless steel cladding layer and the Q235B mild steel substrate layer together, as is shown in Fig. 16. Both component layers were modelled using three-dimensional eight-node reduced integration solid brick elements (C3D8R) with hourglass control. The interfaces between the cladding layer and substrate metal were simulated using a surface-based coupling constraint provided by ABAQUS, called TIE constraint. The effects of residual stresses and geometric imperfections were not involved in the model. Different displacement spectrums were applied at the ends of the specimens for modelling different cyclic loading protocols.

For modelling the material behaviour of each component layers under cyclic loading, the Chaboche's cyclic constitutive model mentioned in the previous section was also used herein. Two cyclic coupon specimens of the pure 316L austenitic stainless steel and Q235B mild steel were machined from the SC bimetallic specimen. They were tested under the cyclic loading protocol LP3 to provide the experimental cyclic stress-strain curves for calibrating the constitutive model parameters for each component layer material. Fig. 17 shows the experimental cyclic loading test results for the pure 316L austenitic stainless steel and Q235B mild steel. It should be noted that both tests were terminated once the obvious buckling was observed. The 316L austenitic stainless steel exhibited larger maximum cyclic tensile stress and slightly thinner

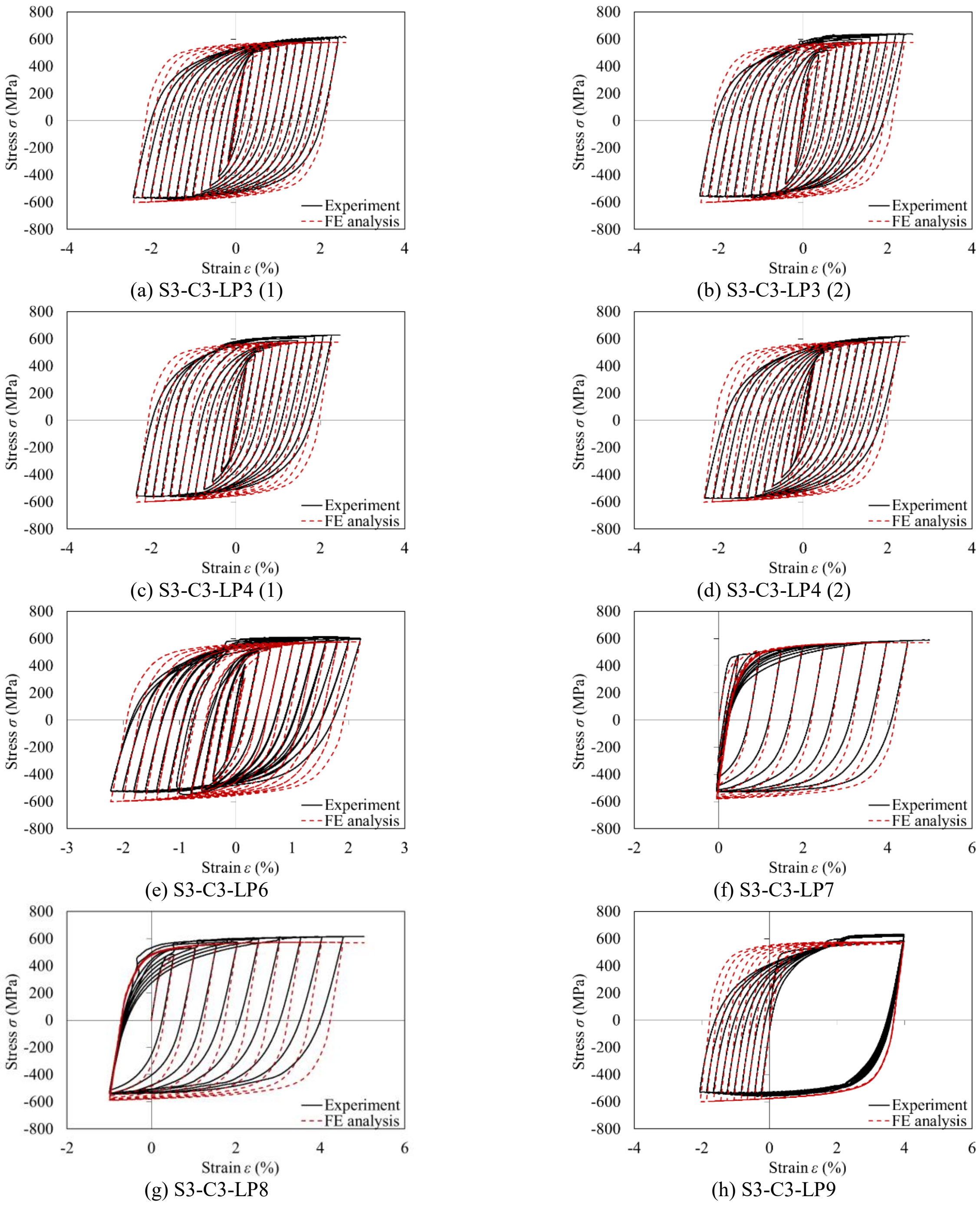

(a) S3-C3-LP3 (1) (b) S3-C3-LP3 (2) (c) S3-C3-LP4 (1) (d) S3-C3-LP4 (2) (e) S3-C3-LP6 (f) S3-C3-LP7 (g) S3-C3-LP8 (h) S3-C3-LP9

Continued-

cyclic curve compared with the Q235B mild steel, although the increase of its cyclic compressive stresses was suppressed due to the early occurrence of local bucking on such a thin specimen. Table 5 lists the calibrated parameters of the constitutive model for the pure 316L austenitic stainless steel and Q235B mild steel. These parameter values were inputted into the cyclic constitutive model for each component layer material in the FE model for simulating the cyclic behaviour of the SC bimetallic steels.

Figs. 18 and 19 shows the comparisons of the cyclic stress-strain curves from the developed two-layer FE model and experimental tests for the SC bimetallic steels with β = 0.5 and 0.375, respectively. 15 cyclic loading protocols were considered. It can be seen that the cyclic stress-strain curves obtained from the two-layer FE model have satisfactory agreement with the experimental results, although some of the curves from the FE model are a little plumber than the experimental ones, which could be because the loading eccentricity on the coupon specimens

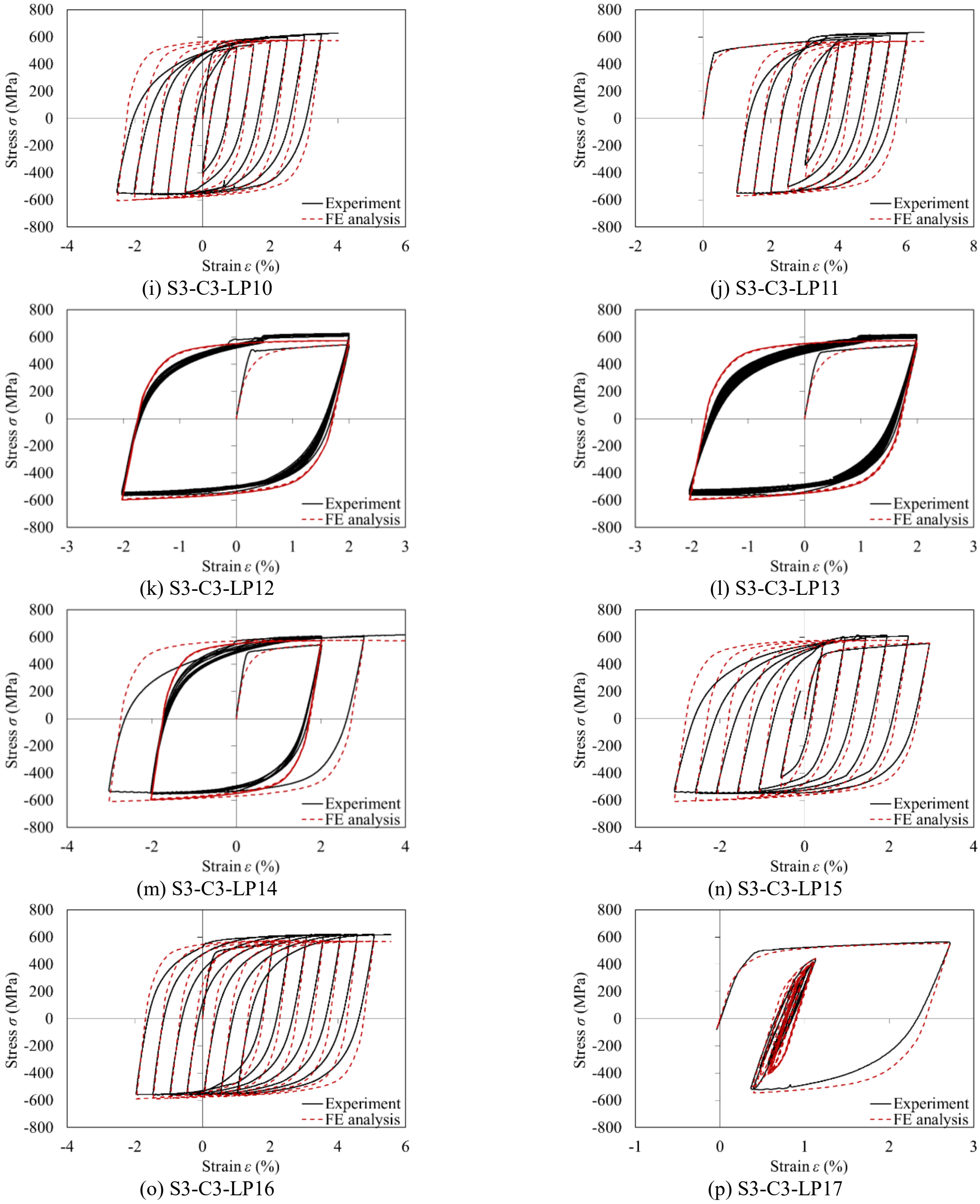

Fig. 18 Comparisons of cyclic curves obtained by using two-layer FE model and from experimental tests for SC bimetallic steels with β = 0.5

cannot be eliminated completely in the experiment due to the existence of initial geometric imperfections in the specimens, or because of the occurrence of local buckling on the specimens during the experimental testing. In the FE model, the initial geometric imperfections were not considered. Local buckling, which cause the degradation of the strength and stiffness of specimen, was also deliberately avoided, since it corresponded to a failure mode in structural level rather than that in material level. Through the comparisons, the accuracy of the developed two-layer FE model is validated, and it is demonstrated that the developed two-layer FE model is capable of capturing the cyclic behaviour of the SC bimetallic steel materials under different loading protocols.

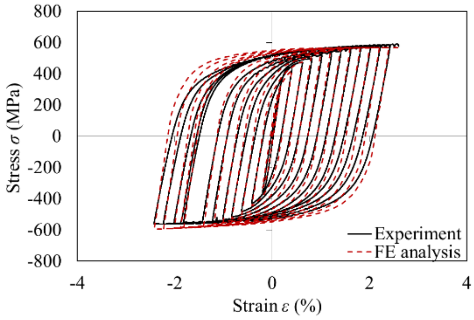

(a) S5-C3-LP3 (1)

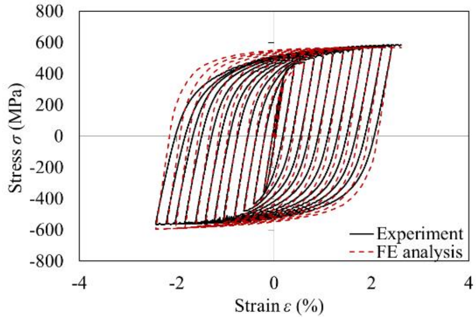

(b) S5-C3-LP3 (2)

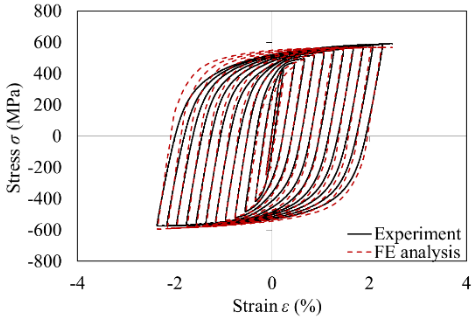

(c) S5-C3-LP4 (1)

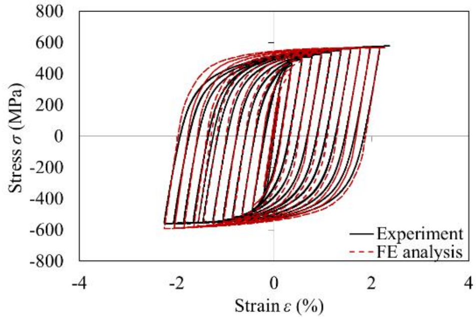

(d) S5-C3-LP5

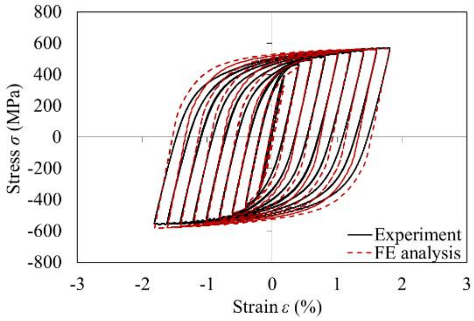

(e) S5-C3-LP6

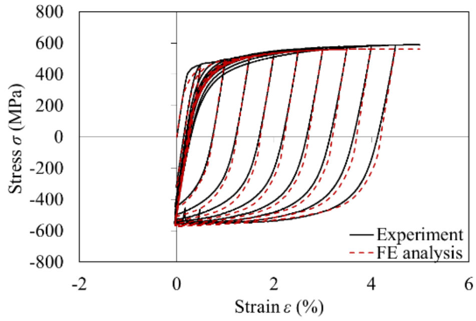

(f) S5-C3-LP7

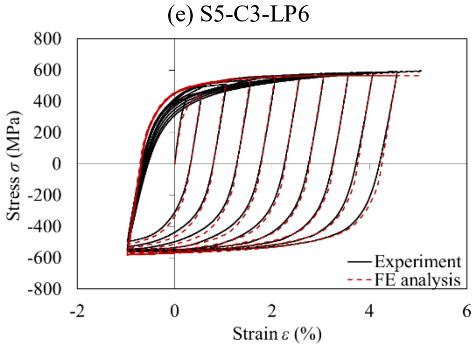

(g) S5-C3-LP8

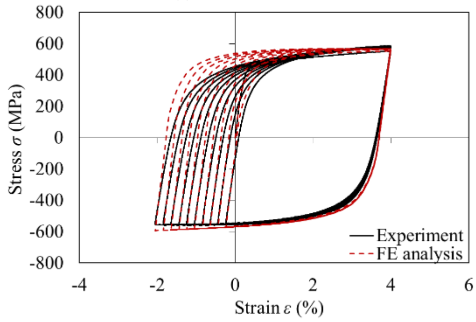

(h) S5-C3-LP9

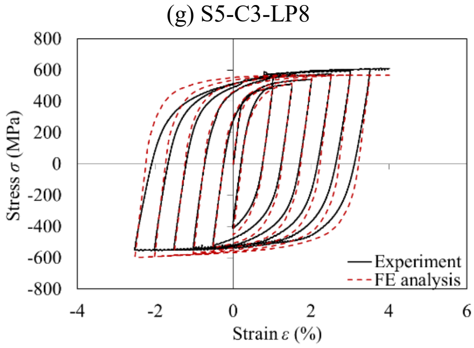

(i) S5-C3-LP10

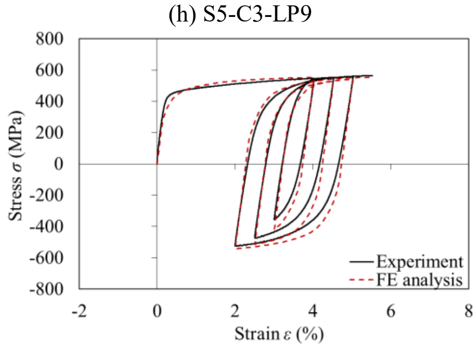

(j) S5-C3-LP11

Continued-

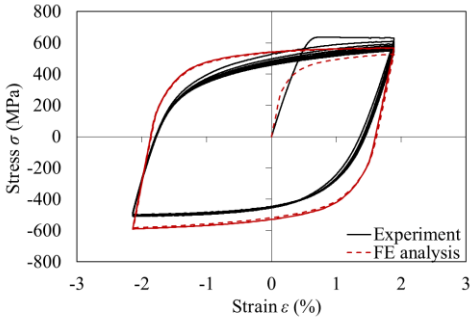

(k) S5-C3-LP12

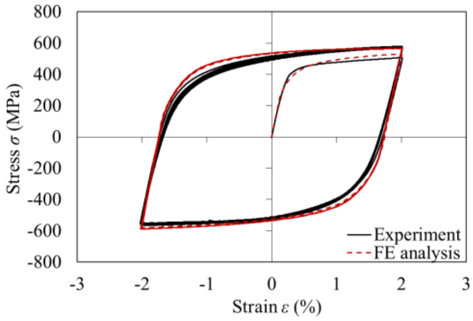

(l) S5-C3-LP13

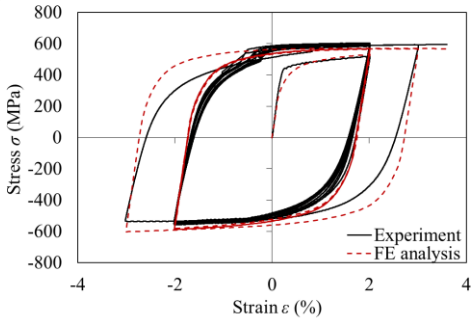

(m) S5-C3-LP14

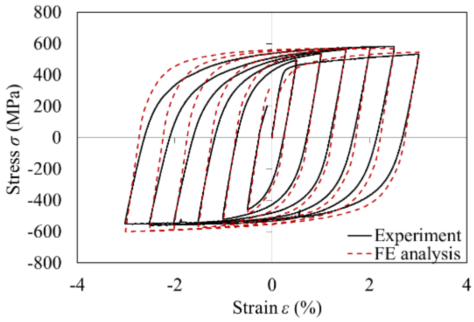

(n) S5-C3-LP15

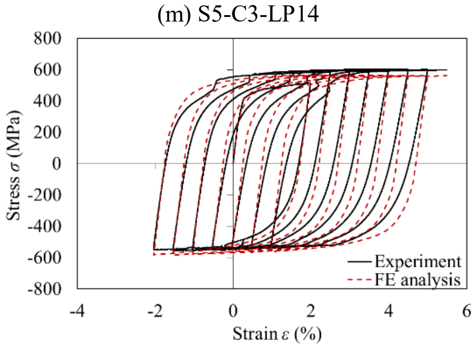

(o) S5-C3-LP16

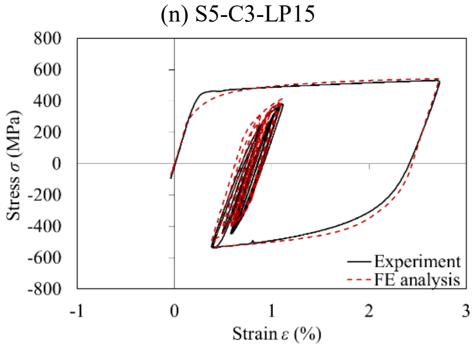

(p) S5-C3-LP17

Fig. 19 Comparisons of cyclic curves obtained by using two-layer FE model and from experimental tests for SC bimetallic steels with $\beta = 0.375$

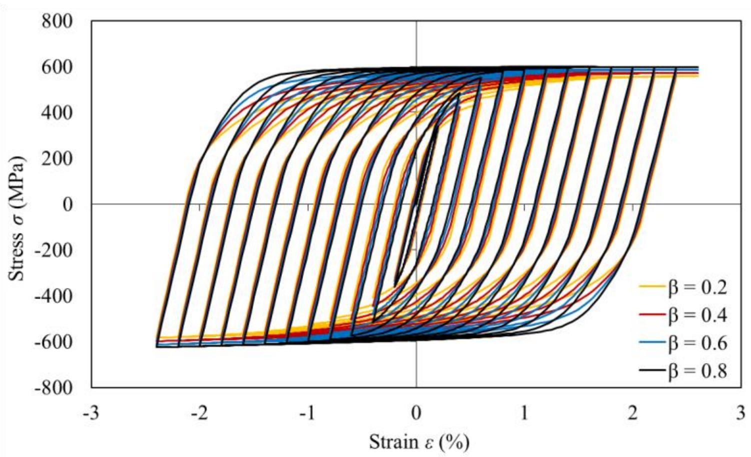

Fig. 20 Comparisons of cyclic curves obtained using two-layer FE model for SC bimetallic steels with various clad ratio

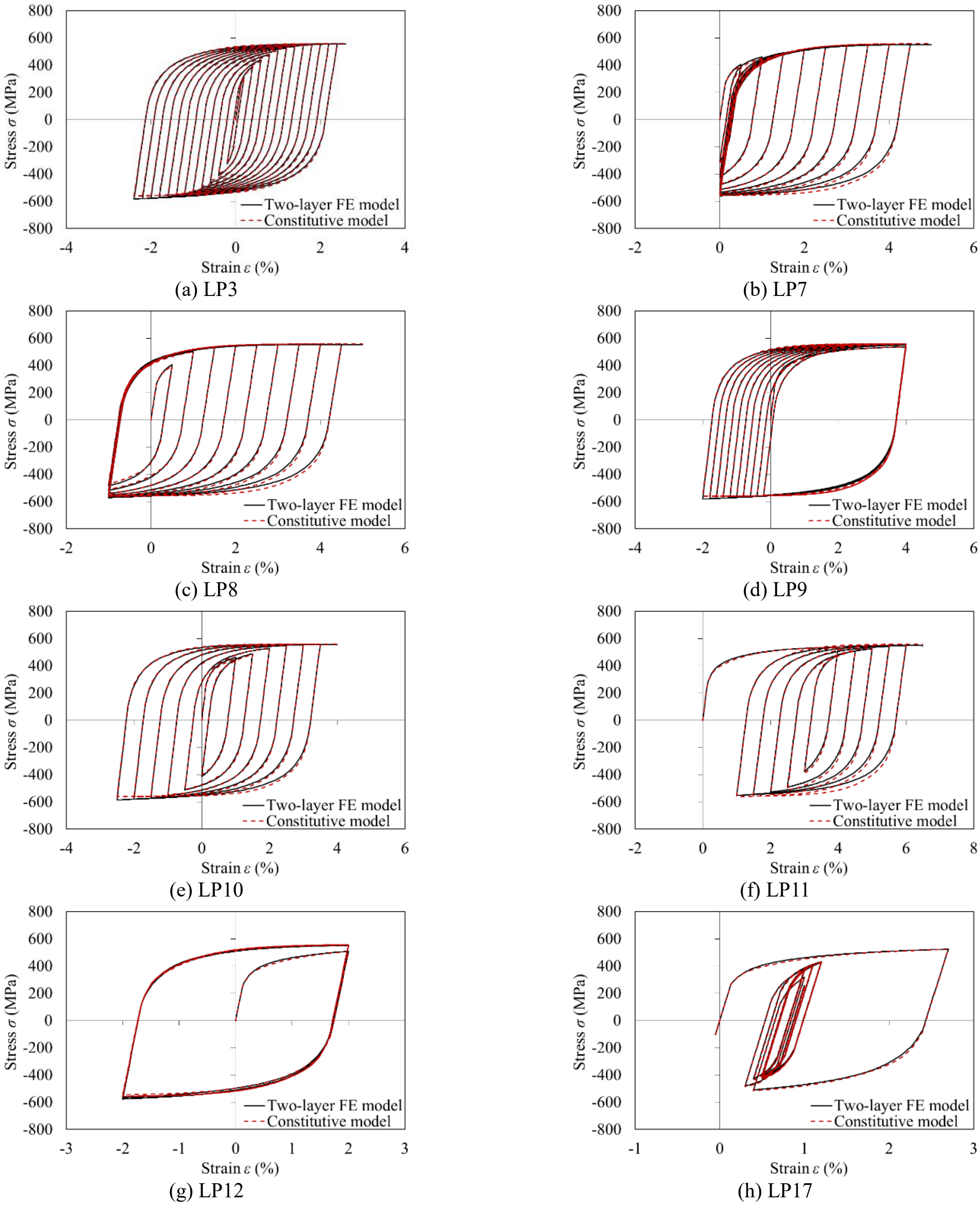

Fig. 21 Comparisons of cyclic curves obtained by using single-layer FE model based on recommended constitutive model and by using two-layer FE model for SC bimetallic steels with $\beta = 0.2$

3.3 Calibrations of constitutive model parameters for SC bimetallic steels

By using the validated two-layer FE model, the cyclic stress-strain curves of 11 SC bimetallic steels with different clad ratios β varied from 0 to 1 were analysed. In these FE analyses, the elastic modulus of the Q235B steel is taken as 206 GPa based on the Chinese standard GB 50017 (2017) while that of the 316L austenitic stainless steel is assumed to be 193 GP as suggested by the specification CECS410 (2015). The values of the other constitutive model parameters for each component layer material adopted the values listed in Table 5. Fig. 20 depicts the comparisons of the cyclic stress-strain curves obtained using the two-layer FE model for the SC bimetallic steels with $\beta = 0.2$, 0.4, 0.6 and 0.8 under the loading protocol LP3. The consistent observations can be recognised from the FE analysis results and the experimental ones described previously. It can be seen that the change in the clad ratio has significant influence on the cyclic behaviour of the SC bimetallic steels.

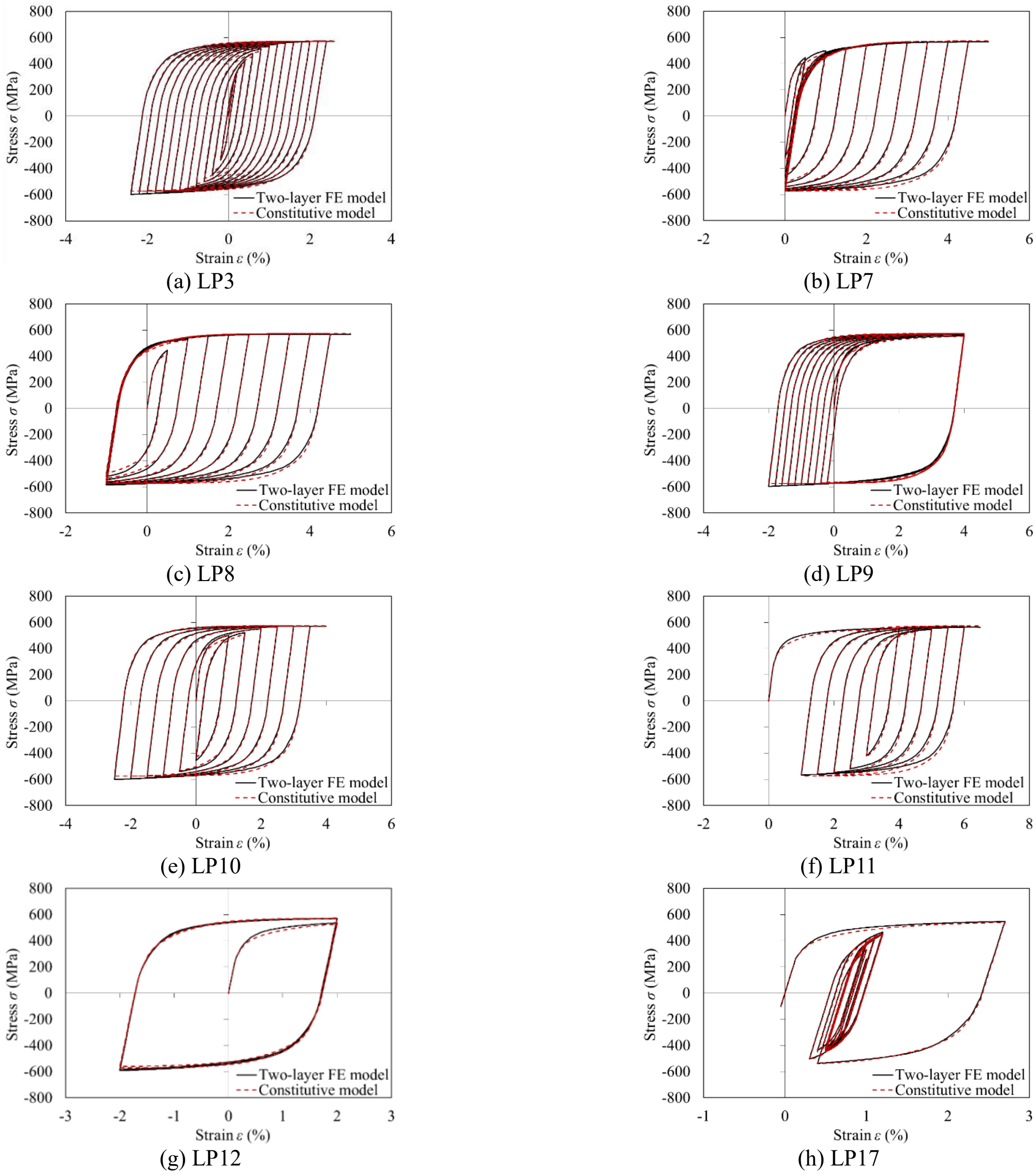

(a) LP3 (b) LP7 (c) LP8 (d) LP9 (e) LP10 (f) LP11 (g) LP12 (h) LP17

Fig. 22 Comparisons of cyclic curves obtained by using single-layer FE model based on recommended constitutive model and by using two-layer FE model for SC bimetallic steels with $\beta = 0.4$

Table 6 Calibrations of constitutive model parameters for SC bimetallic steels with various clad ratios

β	E (GPa)	$\sigma\|_0$ (MPa)	Q_∞ (MPa)	b	C_1 (MPa)	γ_1	C_2 (MPa)	γ_2	S (MPa)
0	206.0	264.0	74	34	17841	109	63794	1436	546.1
0.1	204.7	264.6	74	34	17600	108	54000	980	556,7
0.2	203.4	265.2	70	34	20746	136	68600	940	560.7
0.3	202.1	265.8	67	34	20100	140	98900	1070	568.8
0.4	200.8	266.4	66	34	23192	164	134615	1340	574.3
0.5	199.5	267.0	63	34	26900	190	185000	1650	583.7
0.6	198.2	267.6	110	2800	34420	330	34420	330	586.2
0.7	196.9	268.2	113	2800	44000	420	44000	420	590.7
0.8	195.6	268.8	114	2800	53760	496	53760	496	599.6
0.9	194.3	269.4	115	2800	66400	590	66400	590	609.5
1	193.0	270.0	118	2800	74454	662	74454	662	612.9

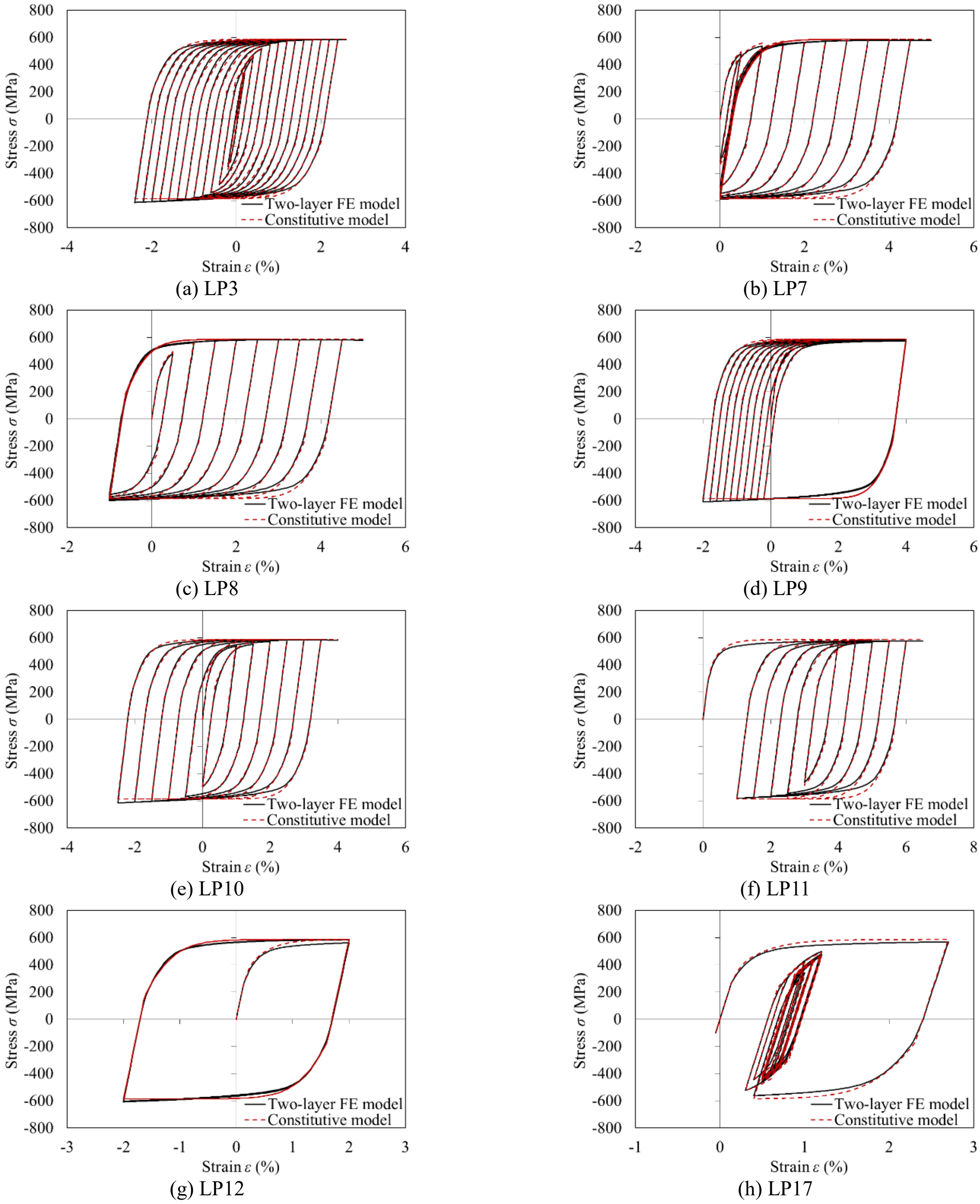

Fig. 23 Comparisons of cyclic curves obtained by using single-layer FE model based on recommended constitutive model and by using two-layer FE model for SC bimetallic steels with $\beta = 0.6$

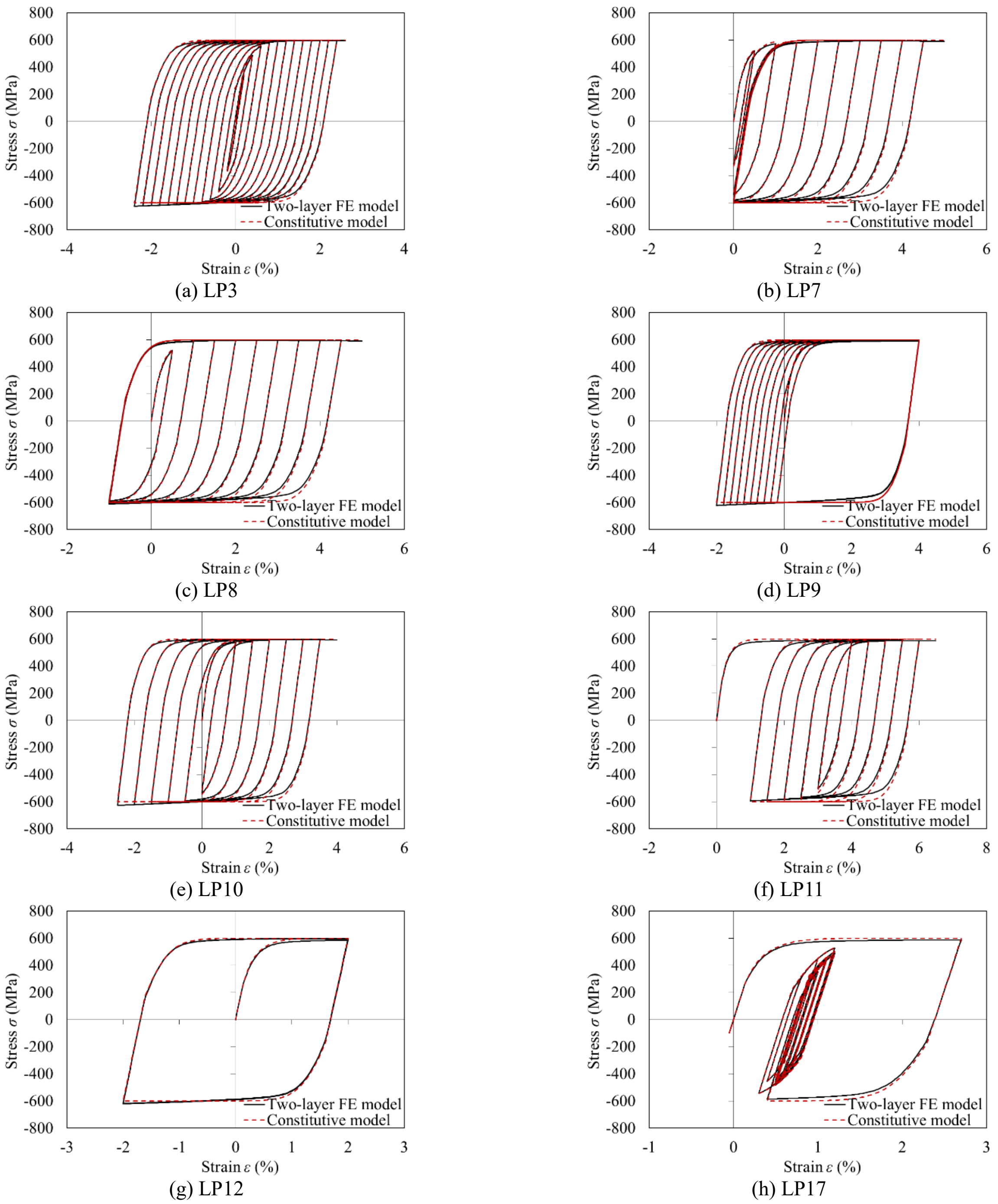

Fig. 24 Comparisons of cyclic curves obtained by using single-layer FE model based on recommended constitutive model and by using two-layer FE model for SC bimetallic steels with $\beta = 0.8$

Based on the FE analysis results obtained using the two-layer FE model for the symmetric strain-controlled cyclic loading protocol LP3, the material parameters of the recommended cyclic constitutive model are calibrated for the 11 SC bimetallic steels with different clad ratios β varied from 0 to 1. All values of the calibrated parameters are summarised in Table 6. It is shown from Table 6 that with an increase in the clad ratio β, the yield stress at zero equivalent plastic strain $\sigma|_0$ increases while the elastic modulus E reduces. When $0 \leq \beta \leq 0.5$, the value of Q_∞ is in the range of 63 to 74. When $0.5 < \beta \leq 0.1$, the value of Q_∞ become much larger and is in the range of 109 to 118, which indicates that the SC bimetallic steels with $0.5 < \beta \leq 1$ exhibit higher degree of isotropic hardening than those with $0 \leq \beta \leq 0.5$. In the last column of Table 6, the values of $S = \sigma|_0 + Q_\infty + C_1/\gamma_1 + C_2/\gamma_2$ are also given. These values represent the maximum changes of the cyclic stresses. It can be seen that the value of S increase almost linearly with an increase of the clad ratio β.

By adopting the recommended cyclic constitutive model with the calibrated parameters, a simplified single-layer FE model is used for simulating the cyclic stress-strain curves of the SC bimetallic steels with various clad ratios. The results of its simulation are compared with the numerical results obtained by using the two-layer FE models for the SC bimetallic steels with various clad ratios under different typical loading protocols. Some of the comparisons are shown in Figs. 21-24. It can be seen that both results have excellent agreement, which verify the accuracy of the recommended cyclic constitutive model with the calibrated parameters for simulating the cyclic behaviour of the SC bimetallic steels with various clad ratios. It should be noted that more further experimental investigations involving more clad ratios are needed for verification due to limited specimens tested herein.

4. Conclusions

An investigation on the cyclic behaviour of the SC bimetallic steels with various clad ratios has been presented in this paper. A series of experimental monotonic and cyclic loading tests on the SC bimetallic steel plate coupon specimens with the clad ratio $\beta = 0.5$ was reported. In the experimental tests, a total of 17 loading protocols including monotonic tensile and compressive loadings as well as 15 different cyclic loading protocols were adopted. The monotonic and cyclic stress-strain curves of the SC bimetallic steels with $\beta = 0.5$ were obtained and analysed. The experimental results showed that the SC bimetallic steels exhibited good ductility under monotonic tensile loading. For the monotonic stress-strain curve, a typical nonlinear stress-strain curve without noticeable yield plateau was identified. The measured cyclic stress-strain curves indicated the good seismic performance and energy dissipation capacity of the SC bimetallic steels. The hardening behaviour with a combination of isotropic and kinematic hardening was recognised for the SC bimetallic steels under cyclic loading. The cyclic skeleton curves of the SC bimetallic steels which could be simulated by using the Ramberg-Osgood model were obviously different from the monotonic stress-strain curves. By comparing the experimental results reported in this paper with the ones of the SC bimetallic steels with $\beta = 0.375$ provided in the literature, it was found that the change in the clad ratio had significant effects on the monotonic and cyclic behaviour of the SC bimetallic steels.

Based on the experimental observations, the commonly used Chaboche's constitutive model considering the combined isotropic and kinematic hardening behaviour of materials under cyclic loading was recommended for numerical simulation of cyclic behaviour of the SC bimetallic steels. To extend the database for calibrating the material parameters of the constitute model for the SC bimetallic steels with a wide range of clad ratios, a two-layer FE model of the SC bimetallic steel coupons subjected to cyclic loadings was developed and was validated by comparing its results with the experimental results. By using the FE analysis results obtained from the two-layer FE model, the material parameters of the recommended constitute model for the SC bimetallic steels with various clad ratios were calibrated. The accuracy of the recommended constitutive model with the calibrated parameters are then verified by comparing the results of its simulation with the numerical results obtained from the two-layer FE model for several different loading protocols. As is suggested, the recommended constitutive model with the calibrated parameters for the SC bimetallic steels with various clad ratios given in this paper will provide a reference for further numerical simulation and seismic design of structures fabricated from the SC bimetallic steels. With consideration of limitation of experimental specimens with only some specific clad ratios, in the future research work, more experimental studies on the cyclic behaviour of different types of SC bimetallic steels with a wider range of clad ratios should be carried out for further investigation, while specimens subjected to large inelastic strains would also need to be taken into consideration.

Acknowledgments

This work in this paper was financially supported by the National Natural Science Foundation of China (51778329, 51608300) and the National Key R&D Program of China (2018YFC0705500, 2018YFC0705503). The first author was supported through a postdoctoral fellowship provided by an Australian Research Council (ARC) Linkage Project (LP150101196) awarded to the fourth author. All the sources of support are gratefully acknowledged.

References

Averseng, J., Bouchair, A. and Chateauneuf, A. (2017), "Reliability analysis of the nonlinear behaviour of stainless steel cover-plate", *Steel Compos. Struct.*, **25**(1), 45-55. https://doi.org/10.12989/scs.2017.25.1.045.

Baddoo, N.R. (2008), "Stainless steel in construction: a review of research, applications, challenge and opportunities", *J. Constr. Steel Res.*, **64**(11), 1199-1206.

https://doi.org/10.1016/j.jcsr.2008.07.011.
Ban, H.Y, Bai, R.S, Yang, L, and Bai, Y. (2019), "Mechanical properties of stainless-clad bimetallic steel at elevated temperatures", *J. Constr. Steel Res.*, **162**, 105704. https://doi.org/10.1016/j.jcsr.2019.105704.
Ban, H.Y. and Shi, Y.J. (2018), "A innovative high performance steel product for structural engineering: Bi-metallic steel", *Proceedings of the International Conference on Engineering Research and Practice for Steel Construction 2018*, Hong Kong, September.
Ban, H.Y., Shi, Y.J. and Tao, X.Y. (2017), "Use of clad steel in engineering structures", *Proceedings of the 15th East Asia-Pacific Conference on Structural Engineering & Construction*, Xi'an, China, October.
BS 7270:2006 (2006), Metallic materials – Constant amplitude strain controlled axial fatigue – Method of test, British Standards Institution; London, UK.
Cai, Y. and Young, B. (2019), "Experimental investigation of carbon steel and stainless steel bolted connections at different strain rates", *Steel Compos. Struct.*, **30**(6), 551-565. https://doi.org/10.12989/scs.2019.30.6.551.
CECS 410-2015 (2015), Technical specification for stainless steel structure, China Association for Engineering Construction Standardization (CECS); Beijing, China.
Chaboche, J.L. (1986), "Time-independent constitutive theories for cyclic plasticity", *Int. J. Plasticity*, **2**(2), 149-188. https://doi.org/10.1016/0749-6419(86)90010-0.
Chaboche, J.L. (1989), "Constitutive equations for cyclic plasticity and cyclic viscoplasticity", *Int. J. Plasticity*, **5**, 247-302. https://doi.org/10.1016/0749-6419(89)90015-6.
Dai, X. and Lam, D. (2010), "Axial compressive behaviour of stub concrete-filled columns with elliptical stainless steel hollow sections", *Steel Compos. Struct.*, **10**(6), 517-539. https://doi.org/10.12989/scs.2010.10.6.517.
De Matteis, G. Brando, G. and Mazzolani, F. M. (2012), "Pure aluminium: An innovative material for structural application in seismic engineering", *Constr. Build. Mater.*, **26**, 677-686.
Dusicka, P., Itani, A.M. and Buckle, I.G. (2007), "Cyclic response of plate steels under large inelastic strains", *J. Constr. Steel Res.*, **63**, 156-164. https://doi.org/10.1016/j.conbuildmat.2011.06.071.
Feng, R., Zhu, W., Wan, H., Chen, A. and Chen, Y. (2018), "Tests of perforated aluminium alloy SHSs and RHSs under axial compression", *Thin-Wall. Struct.*, **130**, 194-212. https://doi.org/10.1016/j.tws.2018.03.017.
Gardner, L. (2019), "Stability and design of stainless steel structures – Review and outlook", *Thin-Walled Structures*, **141**, 208-216. https://doi.org/10.1016/j.tws.2019.04.019.
GB 50017 (2017), Standard for design of steel structures, Ministry of Housing and Urban-Rural Development of PRC and General Administration of Quality Supervision, Inspection and Quarantine of PRC; Beijing, China.
GB/T 228.1 (2010), Metallic materials - Tensile testing - Part 1: Method of test at room temperature, General Administration of Quality Supervision, Inspection and Quarantine of People's Republic of China (AQSIQ) and Standardization Administration of China (SAC); Beijing, China.
GB/T 700 (2006), Carbon structural steels, General Administration of Quality Supervision, Inspection and Quarantine of People's Republic of China (AQSIQ) and Standardization Administration of China (SAC); Beijing, China.
GB/T 8165 (2008), Stainless steel clad plates, General Administration of Quality Supervision, Inspection and Quarantine of People's Republic of China (AQSIQ) and Standardization Administration of China (SAC); Beijing, China.
Guo, X., Wang, L., Shen, Z., Zou, J. and Liu, L. (2018), "Constitutive model of structural aluminium alloy under cyclic loading", *Constr. Build. Mater.*, **180**, 643-654. https://doi.org/10.1016/j.conbuildmat.2018.05.291.
Guo, X., Xiong, Z., Luo, Y., Qiu, L. and Liu, J. (2015), "Experimental investigation on the semi-rigid behaviour of aluminium alloy gusset joints", *Thin-Wall. Struct.*, **87**, 30-40. https://doi.org/10.1016/j.tws.2014.11.001.
Hai, L.T., Sun, F.F., Zhao, C., Li, G.Q. and Wang, Y.B. (2018), "Experimental cyclic behavior and constitutive modeling of high strength structural steels", *Constr. Build. Mater.*, **189**, 1264-1285. https://doi.org/10.1016/j.conbuildmat.2018.09.028.
Han, L.H., Xu, C.Y. and Tao, Z. (2019), "Performance of concrete filled stainless steel tubular (CFSST) columns and joints: Summary of recent research", *J. Constr. Steel Res.*, **152**, 117-131. https://doi.org/10.1016/j.jcsr.2018.02.038.
He, A. and Zhao, O. (2019), "Experimental and numerical investigations of concrete-filled stainless steel tube stub columns under axial partial compression", *J. Constr. Steel Res.*, **158**, 405-416. https://doi.org/10.1016/j.jcsr.2019.04.002.
He, L., Togo, T., Hayashi, K., Kurata, M. and Nakashima, M. (2016), "Cyclic behaviour of multirow slit shear walls made from low-yield-point-steel", *J. Struct. Eng. - ASCE*, **142**(11), 04016094. https://doi.org/10.1061/(ASCE)ST.1943-541X.0001569.
Hibbit, H.D., Karlsson, B.I. and Sorensen, E.P. (2016), *ABAQUS 2016 User's Manual*, Hibbitt, Karlsson & Sorensen Inc, Pawtucket, Rhode Island, USA.
Ho, H.C., Liu, X., Chung, K.F., Elghazouli, A.Y. and Xiao, M. (2018), "Hysteretic behaviour of high strength S690 steel materials under low cycle high strain tests", *Eng. Struct.*, **165**, 222-236. https://doi.org/10.1016/j.engstruct.2018.03.041.
Hu, F. (2016), "Study on seismic behavior and design method of high strength steel frames", Ph.D. Dissertation, Tsinghua University, Beijing.
Hu, F., Shi, G. and Shi, Y. (2016), "Constitutive model for full-range elasto-plastic behavior of structural steels with yield plateau: Calibration and validation", *Eng. Struct.*, **118**, 210-227. https://doi.org/10.1016/j.engstruct.2016.03.060.
Hu, F., Shi, G. and Shi, Y. (2018), "Constitutive model for full-range elasto-plastic behavior of structural steels with yield plateau: Formulation and implementation", *Eng. Struct.*, **171**, 1059-1070. https://doi.org/10.1016/j.engstruct.2016.02.037.
Huang, Y. and Young, B. (2018), "Design of cold-formed stainless steel circular hollow section columns using direct strength method", *Eng. Struct.*, **163**, 177-183. https://doi.org/10.1016/j.engstruct.2018.02.012.
Javidan, F., Heidarpour, A., Zhao X.L. and Fallahi, H. (2017), "Fundamental behaviour of high strength and ultra-high strength steel subjected to low cycle structural damage", *Eng. Struct.*, **143**, 427-440. https://doi.org/10.1016/j.engstruct.2017.04.041.
Jia, L.J. and Kuwamura, H. (2013), "Prediction of cyclic behaviors of mild steel at large plastic strain using coupon test results", *J. Struct. Eng. - ASCE*, **140**(2), 04013056. https://doi.org/10.1061/(ASCE)ST.1943-541X.0000848.
Li, D., Uy, B., Aslani, F. and Hou, C. (2019), "Behaviour and design of spiral-welded stainless steel tubes subjected to axial compression", *J. Constr. Steel Res.*, **154**, 67-83. https://doi.org/10.1016/j.jcsr.2018.11.029.
Liao, F.Y.., Han, L.H., Tao, Z. and Rasmussen, K.J.R. (2017) "Experimental behavior of concrete filled stainless steel tubular columns under cyclic lateral loading", *J. Struct. Eng. - ASCE*, **143**(4), 04016219. https://doi.org/10.1061/(ASCE)ST.1943-541X.0001705.
Liu, X., Bai, R. Uy, B. and Ban, H. (2019a), "Material properties and stress-strain curves for titanium-clad bimetallic steels", *J. Constr. Steel Res.*, **162**, 105756. https://doi.org/10.1016/j.jcsr.2019.105756
Liu, X., Uy, B. and Mukherjee, A. (2019b), "Transmission of

ultrasonic guided wave for damage detection in welded steel plate structures", *Steel Compos. Struct.*, **33**(3), 445-461. https://doi.org/10.12989/scs.2019.33.3.445

Ma, Z.Y., Hao, J.P. and Yu, H.S. (2018), "Shaking-table test of a novel buckling-restrained multi-stiffened low-yield-point steel plate shear wall", *J. Constr. Steel Res.*, **145**, 128-136. https://doi.org/10.1016/j.jcsr.2018.02.009.

Nip, K.H., Gardner, L., Davies, C.M. and Elghazouli A.Y. (2010), "Extremely low cycle fatigue tests on structural carbon steel and stainless steel", *J. Constr. Steel Res.*, **66**, 96-110. https://doi.org/10.1016/j.jcsr.2009.08.004.

Ramberg, W. and Osgood, W.R. (1943), "Description of stress-strain curves by three parameters", Technical Note No. 902; National Advisory Committee for Aeronautics, Washington, DC, USA.

Shi, G., Gao, Y., Wang, X. and Zhang, Y. (2018), "Mechanical properties and constitutive models of low yield point steels", *Constr. Build. Mater.*, **175**, 570-587. https://doi.org/10.1016/j.conbuildmat.2018.04.219.

Shi, G., Wang, M., Bai, Y., Wang, F., Shi, Y. and Wang, Y. (2012), "Experimental and modeling study of high-strength structural steel under cyclic loading", *Eng. Struct.*, **37**, 1-13. https://doi.org/10.1016/j.engstruct.2011.12.018.

Shi, Y., Wang, M. and Wang, Y. (2011), "Experimental and constitutive model study of structural steel under cyclic loading", *J. Constr. Steel Res.*, **67**, 1185-1197. https://doi.org/10.1016/j.jcsr.2011.02.011.

Silvestre, E., Mendiguren, J., Galdos, L. and De Argandoña, E.S. (2015), "Comparison of the hardening behaviour of different steel families: From mild and stainless steel to advanced high strength steels", *Int. J. Mech. Sci.*, **101-102**, 10-20. https://doi.org/10.1016/j.ijmecsci.2015.07.013.

Sim, J.C. and Hughes, T.J.R. (1998), Computational Inelasticity, Springer-Verlag Inc, New York, NY, USA.

Smith, L. (2012), "Engineering with clad steel, 2nd Edition", *Nickel Institute Technical Series N0*, **10064**, 1-24.

Su, M.-N., Young, B. and Gardner, L. (2014), "Deformation-based design of aluminium alloy beams", *Eng. Struct.*, **80**, 339-349. https://doi.org/10.1016/j.engstruct.2014.08.034.

Su, M.-N., Zhang, Y. and Young, B. (2019), "Design of aluminium alloy beams at elevated temperatures", *Thin-Wall. Struct.*, **140**, 506-515. https://doi.org/10.1016/j.tws.2019.03.052.

Theofanous M. and Gardner, L. (2012), "Effect of element interaction and material nonlinearity on the ultimate capacity of stainless steel cross-sections", *Steel Compos. Struct.*, **12**(1), 73-92. https://doi.org/10.12989/scs.2012.12.1.073

Usami, T., Gao, S. and Ge, H. (2000), "Elastioplastic analysis of steel members and frame subjected to cyclic loading", *Eng. Struct.*, **22**, 135-145. https://doi.org/10.1016/S0141-0296(98)00103-5.

Wang, J., Uy, B. and Li, D. (2019), "Behaviour of large fabricated stainless steel beam-to-tubular column joints with extended endplates", *Steel Compos. Struct.*, **32**(1), 141-156. https://doi.org/10.12989/scs.2019.32.1.141.

Wang, M., Fahnestock, L.A., Qian, F. and Yang, W. (2017), "Experimental cyclic behavior and constitutive modeling of low yield point steels", *Constr. Build. Mater.*, **131**, 696-712. https://doi.org/10.1016/j.conbuildmat.2016.11.035.

Wang, Y.B., Li, G.Q., Cui, W., Chen, S.W. and Sun, F.F. (2015), "Experimental investigation and modeling of cyclic behavior of high strength steel", *J. Constr. Steel Res.*, **104**, 37-48. https://doi.org/10.1016/j.jcsr.2014.09.009.

Wang, Y.Q., Chang, T., Shi, Y.J., Yuan, H.X., Yang, L. and Liao, D.F. (2014), "Experimental study on the constitutive relation of austenitic stainless steel S31608 under monotonic and cyclic loading", *Thin-Wall. Struct.*, **83**, 19-27. https://doi.org/10.1016/j.tws.2014.01.028.

Xu, L., Nie, X., Fan, J., Tao, M. and Ding, R. (2016), "Cyclic hardening and softening behavior of the low yield point steel BLY160: Experimental response and constitutive modeling", *Int. J. Plasticity*, **78**, 44-63. https://doi.org/10.1016/j.ijplas.2015.10.009.

Xu, L.Y., Nie, X. and Fan, J.S. (2016), "Cyclic behaviour of low-yield-point-steel shear panel dampers", *Eng. Struct.*, **126**, 391-404. https://doi.org/10.1016/j.engstruct.2016.08.002.

Yang, L., Zhao, M., Chan, T.M., Shang, F. and Xu, D. (2016), "Flexural buckling of welded austenitic and duplex stainless steel I-section columns", *J. Constr. Steel Res.*, **122**, 339-353. https://doi.org/10.1016/j.jcsr.2016.04.007.

Yousefi, A.M., Lim, J.B.P., Uzzaman, A., Lian, Y., Clifton, G.C. and Young, B. (2016), "Web crippling strength of cold-formed stainless steel lipped channel-sections with web openings subjected to interior-one-flange loading condition", *Steel Compos. Struct.*, **21**(3), 629-659. https://doi.org/10.12989/scs.2016.21.3.629.

Zhou, F., Chen, Y. and Wu, Q. (2015), "Dependence of the cyclic response of structural steel on loading history under large inelastic strains", *J. Constr. Steel Res.*, **104**, 64-73. https://doi.org/10.1016/j.jcsr.2014.09.019.

Zhou, F. and Li, L. (2016), "Experimental study on hysteretic behavior of structural stainless steel under cyclic loading", *J. Constr. Steel Res.*, **122**, 94-109. https://doi.org/10.1016/j.jcsr.2016.03.006

Zhu, J.C., Ban, H.Y., Shi, G. and Zhang, Y. (2018), "Cyclic tests of stainless-clad steel plates", *Proceedings of the International Conference on Engineering Research and Practice for Steel Construction 2018*, Hong Kong, China, September.

Zirakian, T. and Zhang, J. (2015), "Structural performance of unstiffened low yield point steel plate shear wall", *J.Constr. Steel Res.*, **112**, 40-53. https://doi.org/10.1016/j.jcsr.2015.04.023.

DL